A mimetic tensor artificial viscosity for Lagrangian hydrocodes on arbitrary polygonal meshes LA-UR-10-00006

K.Lipnikov*† M.Shashkov*

January 7, 2010

Abstract

We construct a new mimetic tensor artificial viscosity on general polygonal meshes. The tensor viscosity is designed as a mimetic discretization of the differential operator div $(\mu\nabla\mathbf{u})$. This discretization includes the case of a full tensor coefficient μ. We prove that the new tensor viscosity preserves symmetry on special meshes. We demonstrate performance of the new viscosity for the Noh implosion, Sedov explosion and Saltzman piston problems on a set of various polygonal meshes in both Cartesian and axisymmetric coordinate systems.

1 Introduction

We are developing advanced mimetic discretizations methods for Lagrangian gasdynamics on general polygonal meshes in both Cartesian (x, y) and axisymmetric (r, z) coordinate systems. Our particular interest is in modeling complex high-speed flows with shocks. Modeling of such flows requires introduction of an artificial numerical viscosity [12]. This paper is mainly devoted to development of a new mimetic artificial viscosity on general polygonal meshes.

For a brief historical overview and basic requirements for design of artificial viscosity methods, we refer the interested reader to [12] and focus our attention on a special class of viscosity methods. The *tensor artificial viscosity* was proposed in [11]. This viscosity is designed as a discretization of the differential operator div $(\mu\nabla\mathbf{u})$. In [11], the authors considered only the case of a scalar coefficient μ and a computational mesh consisting of convex polygonal cells.

In the recent paper [21], the authors derived a high-order discretization for the tensor viscosity using a finite-element approach. This approach is applicable only to non-degenerate quadrilateral meshes in two-dimensions and non-degenerate hexahedral meshes in three-dimensions. Again, only a scalar μ was considered in [21]. Still, the numerical results

*Los Alamos National Laboratory, MS B284, Los Alamos, NM 87545, {lipnikov,shashkov}@lanl.gov
†Corresponding author

presented in [11, 21] clearly demonstrate superiority of the tensor artificial viscosity over other known forms of the artificial viscosity.

In a real computation, one can easily encounter meshes produced by an adaptive mesh refinement (AMR), where angles between edges sharing a vertex can be equal to π, as well as meshes with non-convex cells. The methods proposed in [11, 21] are not designed to work for such meshes. What is even more important, is that the discrete formulas derived in [11, 21] have a singularity when the angle between two edges sharing a vertex approaches π, which may lead to computational instabilities. Therefore, our *first objective* is to develop a robust discretization of the differential operator $\mathrm{div}\,(\mu\nabla\mathbf{u})$ that works on general polygonal meshes with degenerate and non-convex cells.

One of the important features of the tensor viscosity is its ability to catch direction of the shock propagation. This is achieved because $\nabla\mathbf{u}$ is the true tensor. Directional properties of the tensor artificial viscosity also allows to introduce special limiters, which turn viscosity off for adiabatic compression. This may be very important for implosion problems [12].

There are still a few open problems related to definition of coefficient μ. One of them is selection of a characteristic length, especially for highly stretched cells, which controls thickness of the discrete shock. In this respect, a full fourth-order tensor coefficient μ has enormous potential, provided that a discretization can handle such a tensor. Therefore, our *second objective* is to develop a discretization of the differential operator $\mathrm{div}\,(\mu\nabla\mathbf{u})$ with the tensor coefficient μ.

In first part of this paper, we develop a new mimetic discretization of the operator $\mathrm{div}\,(\mu\nabla\mathbf{u})$ in the Cartesian (x, y) coordinate system. The coefficient μ can be a full fourth-order symmetric positive semi-definite tensor. The new discretization is based on ideas developed over the last decade in the framework of mimetic finite difference (MFD) methods [19, 18, 16, 24, 17, 10, 3].

In the traditional MFD method, one first discretizes the first-order operators ∇, div (see, for example, [11, 10]) and then forms a discrete analog of the second-order operator $\mathrm{div}\,(\mu\nabla\mathbf{u})$. In context of constructing a tensor artificial viscosity, we do not need the discrete first-order operators *per se*, we only need a discretization of the second-order operator, because it is the one who provides artificial viscosity forces in the momentum equation.

The main new idea is the direct discretization of the second-order operator $\mathrm{div}\,(\mu\nabla\mathbf{u})$. This is done by specifying an inner product in a space of tensors on its subspace. This subspace consists of tensors that are gradients of the vectors. This construction can be considered as an extension of ideas presented in [3] for the scalar Laplacian to the case of tensors. It also makes important contribution to the theory of the discrete vector and tensor calculus which we are developing [19, 18, 15, 4, 5, 22, 16, 24, 17, 10, 23].

In the second part of the paper, we describe how to incorporate the tensor artificial viscosity into the discrete Lagrangian hydrodynamics. In this part, we use only a scalar coefficient μ. Construction of a tensor coefficient μ, in the context of Lagrangian hydrodynamics, will be a topic of a future paper. To construct a conservative discretization of Lagrangian equations, we use the compatible discretization technique from [13].

We start with the two-dimensional Cartesian geometry. In this case, we use directly the artificial viscosity constructed in the first part of this paper. For the axisymmetric geometry, we use the "area-weighted" approach (see, for example, [13, 2]). In this approach, forces in the right-hand side of the momentum equation are discretized exactly as in the Cartesian

geometry; however, a special procedure is required to approximate density in the left-hand side. We stress once more that the same discretization of the operator $\operatorname{div}(\mu\nabla\mathbf{u})$ is used in both coordinate systems.

One of the desired properties for the discrete equations is preservation of symmetry on special meshes. We develop a methodology based on a *reference element*, which allows us to analyze and to prove symmetry on special meshes without explicit form of the discrete equations. Using this methodology, we prove that our discretization preserves cylindrical symmetry in the Cartesian geometry and spherical symmetry in the axisymmetric geometry on equiangular polar meshes, subject to appropriate initial and boundary conditions.

The new tensor artificial viscosity has been implemented in the code FLAG [7, 8, 9]. Our test suite includes the Noh implosion problem [25], the Sedov blast wave problem [20, 27, 28], and the Saltzman piston problem [26, 14]. Noh's and Sedov's problems are tested on several meshes: polar meshes with uniform and non-uniform angular steps; square and rectangular meshes; a polar mesh with adaptive mesh refinement; and a general polygonal mesh. Results of numerical tests demonstrate accuracy and robustness of the new tensor artificial viscosity. They also confirm that the new method preserves cylindrical and spherical symmetry on polar equiangular meshes and show how symmetry is violated on other meshes.

The paper outline is as follows. In Section 2, we set the stage by describing how continuous analog of the tensor artificial viscosity enters equations of Lagrangian gasdynamics. Semi-discrete equations in the Cartesian geometry are described in Section 3. It includes a brief description of the compatible staggered discretization. Main part of this section is devoted to derivation of the new tensor artificial viscosity. In Section 4, we describe briefly the area-weighted discretization for the axisymmetric geometry. Analysis of symmetry preservation is performed in Section 5. Numerical investigation of approximation properties of the mimetic discretization of operator $\operatorname{div}(\mu\nabla\mathbf{u})$ is done in Section 6. Finally, results of numerical experiments are presented in Section 7.

2 Continuous equations of Lagrangian gasdynamics

Let us consider a system of hydrodynamics equations in Lagrangian coordinates describing motion of a compressible gas [29]. The first equation comes from the conservation law for mass:

$$\frac{1}{\rho}\frac{D\rho}{Dt} = -\operatorname{div}\mathbf{u},$$

where ρ is a gas density, $\mathbf{u}$ is the gas velocity, and D/Dt denotes the material derivative. The second equation comes from the conservation low for momentum:

$$\rho\frac{D\mathbf{u}}{Dt} = -\nabla \mathrm{p},$$

where p is the gas pressure. The third equation comes from the conservation law for the total energy. The equation for the internal energy density ε reads:

$$\rho\frac{D\varepsilon}{Dt} = -\mathrm{p}\operatorname{div}\mathbf{u}.$$

The system of three equations with four unknowns is closed by an equation of state:

$$\mathrm{p} = \mathrm{p}(\varepsilon, \rho).$$

The ideal gas law is used in our numerical experiments.

2.1 Artificial viscosity

For shock calculations, an artificial numerical viscosity has to be added to the discrete momentum equation. Being artificial, the discrete viscosity stress tensor does not need to be symmetric. Following [11, 21], we define the artificial viscosity as an approximation of the elliptic operator:

$$\tilde{\mathbf{f}}^{vis} = \mathrm{div}\,(\mu \nabla \mathbf{u}),$$

where, contrary to [11, 21], we allow μ be a *fourth-order* tensor. The continuous form of the modified momentum equation (3.2) becomes

$$\rho \frac{D\mathbf{u}}{Dt} = -\nabla \mathrm{p} + \mathrm{div}\,(\mu \nabla \mathbf{u}),$$

or

$$\rho \frac{D\mathbf{u}}{Dt} = \tilde{\mathbf{f}}^{prs} + \tilde{\mathbf{f}}^{vis}, \qquad \tilde{\mathbf{f}}^{prs} = -\nabla \mathrm{p}, \quad \tilde{\mathbf{f}}^{vis} = \mathrm{div}\,(\mu \nabla \mathbf{u}),$$

where $\tilde{\mathbf{f}}^{prs}$ and $\tilde{\mathbf{f}}^{vis}$ are viscous forces due to pressure and artificial viscosity, respectively.

The continuous form of equation for the internal energy which includes work done by the artificial viscosity is

$$\rho \frac{D\varepsilon}{Dt} = -\mathrm{p}\,\mathrm{div}\,\mathbf{u} + \mu\,\nabla\,\mathbf{u} : \nabla\,\mathbf{u}\,.$$

3 Semi-discrete equations of Lagrangian gasdynamics

Let us consider a polygonal partition Ω_h of a computational domain Ω into non-overlapping zones z. We allow Ω_h to contain non-convex and degenerate (a vertex lies on a line connecting two other vertexes) zones. However, we assume that this partition is conformal in the following sense. Intersection of two different zones is either a few mesh points, or a few mesh edges (two adjacent zones may share more than one edge), or empty.

3.1 The $x - y$ coordinate system

Let A_z be the area of zone z and L_e be the length of edge e. We denote by $\mathbf{n}_z$ be the exterior normal vector to boundary ∂z and by $\mathbf{n}_z^e$ its restriction to edge e. We shall frequently write $\mathbf{n}^e$ instead of $\mathbf{n}_z^e$ whenever it will not be ambiguous. Let $\mathbf{x}_z$ be the centroid of zone z and $\mathbf{x}_e$ be the center of edge e.

We consider a staggered discretization. The discrete velocity unknowns $\mathbf{u}_p$ are defined at mesh nodes p. Let $\mathbf{U}$ the the vector of degrees of freedom $\mathbf{u}_p$. The size of this vector is twice the number of mesh points.

For a given vector $\mathbf{U}$, we may reconstruct a continuous discrete function $\mathbf{u}_h$, $\mathbf{u}_h = \mathcal{L}(\mathbf{U})$. We assume that $\mathbf{u}_h$ is linear on every edge e and $\mathbf{u}_h(p) = \mathbf{u}_p$ at every mesh point p. We do not specify the value of $\mathbf{u}_h$ inside zone z, because, as we will see later, it is not needed in our method. In general, the reconstruction operator $\mathcal{L}$ in not unique.

Furthermore, we assume that the reconstruction operator $\mathcal{L}$ is exact for piecewise linear functions in the following sense. Let $\mathbf{u}_L$ be a velocity function linear in each zone z and $\mathbf{U}_L$ be the vector of degrees of freedom. Then, we require that $\mathbf{u}_L = \mathcal{L}(\mathbf{U}_L)$.

The discrete pressure unknowns p_z, density unknowns ρ_z and internal energy unknowns ε_z are defined at centers of zones z. These unknowns define in a natural way piecewise constant mesh functions p_h, ρ_h and ε_h.

For Lagrangian methods, the mass m_z in element z is constant in time and the discrete equation for conservation of mass is

$$\rho_z = \frac{m_z}{A_z}. \tag{3.1}$$

We use a compatible (mimetic) discretization of the momentum and internal energy equations [13]. Let m_p be the constant mass associated with point p and $\mathbf{f}_z^p$ be a subzonal force acting from zone z to point p. Then, the semi-discrete equations are:

$$m_p \frac{D\mathbf{u}_p}{Dt} = \sum_{z \ni p} \mathbf{f}_z^p, \qquad m_z \frac{D\varepsilon_z}{Dt} = -\sum_{p \in z} \mathbf{f}_z^p \cdot \mathbf{u}_p. \tag{3.2}$$

We use the Euler-trapezoidal predictor-corrector method for time integration [13]. To calculate the point masses, we consider a dual mesh $\mathcal{D}_h$ obtained by connecting centers of zones z with mid-points of edges e. This introduces another polygonal partition of the computational domain Ω into dual zones E_p associated with points p. Then the point mass m_p is defined by integrating piecewise constant function ρ_h over the dual zone E_p.

Contribution to the subzonal force $\mathbf{f}_z^p$ from the pressure is defined via the Green formula for dual zone E_p:

$$-\int_{E_p} \nabla \mathrm{p} \, \mathrm{d}A = -\oint_{\partial E_p} \mathrm{p} \, \mathbf{n}_{E_p} \, \mathrm{d}L = -\sum_{z \in p} \int_{\partial E_p \cap z} \mathrm{p} \, \mathbf{n}_{E_p} \, \mathrm{d}L = \sum_{z \in p} \int_{\partial z \cap E_p} \mathrm{p} \, \mathbf{n}_z \, \mathrm{d}L.$$

In the last step we used the fact that boundaries $\partial E_p \cap z$ and $\partial z \cap E_p$ make a closed contour. Replacing p with the discrete function p_h, we get contribution of the pressure to the subzonal point force:

$$(\mathbf{f}^{prs})_z^p = \int_{\partial z \cap E_p} \mathrm{p}_h \, \mathbf{n}_z \, \mathrm{d}L. \tag{3.3}$$

Contribution $(\mathbf{f}^{vis})_z^p$ of the artificial viscosity to the subzonal point force is defined in the next subsection. After that, the scheme is completed by setting

$$\mathbf{f}_z^p = (\mathbf{f}^{prs})_z^p + (\mathbf{f}^{vis})_z^p. \tag{3.4}$$

3.2 Artificial viscous subzonal force

The major focus of this article is on discretization of the artificial viscous term on arbitrary polygonal meshes. As it was mentioned in the previous section, the artificial viscosity contributes to the subzonal point force $\mathbf{f}_z^p$ (see (3.4)). Derivation of the subzonal point force

$(\mathbf{f}^{vis})_z^p$ requires to discretize the vector elliptic operator $\mathrm{div}\,(\mu\nabla\,)$. The presented method is based on the principles of mimetic discretization for the scalar Laplacian [3] but differs from the one in [11]. The novel method can be applied to a larger family of meshes, including meshes with non-convex and degenerate zones, and full tensor coefficient μ.

In the mimetic methodology the combined operator $\mathrm{div}\,\mu$ and the gradient operator ∇ are replaced by compatible discrete mimetic operators $\mathcal{DIV}_\mu$ and $\mathcal{GRAD}$, respectively. A force due to artificial viscosity is calculated as follows:

$$\mathbf{F}^{vis} = -\mathbf{M}_Q\,\mathcal{DIV}_\mu\,\mathcal{GRAD}\;\mathbf{U}, \tag{3.5}$$

where $\mathbf{U}$ is the global vector of velocity degrees of freedom, and the mass matrix $\mathbf{M}_Q$ is introduced below. The matrix $\mathbf{M}_Q$ reflects the fact that the forces are applied to nodal masses (compare with the differential form of the momentum equation). In the sequel, we will show how the vector $\mathbf{F}^{vis}$ can be assembled from subzonal point forces $(\mathbf{f}^{vis})_z^p$ without explicit calculation of the mimetic operators. However, the basis of the mimetic discretization has to be introduced first. To simplify exposition, we assume the following boundary conditions on $\partial\Omega$:

$$\mathbf{u}\cdot\mathbf{n} = 0 \qquad \text{and} \qquad (\nabla\mathbf{u}\cdot\mathbf{n})\cdot\boldsymbol{\tau} = 0, \tag{3.6}$$

where $\mathbf{n}$ and $\boldsymbol{\tau}$ are the unit normal and tangential vectors, respectively.

Let Q^h be the space of velocity vectors $\mathbf{V}$. The dimension of this space is twice the number of mesh nodes. The vector $\mathbf{V}\in Q^h$ is composed of two-dimensional vectors $\mathbf{v}_p$ (denoted also as $(\mathbf{V})^p$) where p is a mesh point. The boundary condition (3.6) implies that $(\mathbf{V})^p\cdot\mathbf{n} = 0$ for every boundary point p. The space Q^h is equipped with the inner product:

$$[\mathbf{U},\,\mathbf{V}]_Q \equiv (\mathbf{M}_Q\mathbf{U})^T\,\mathbf{V}, \qquad \forall\mathbf{U},\mathbf{V}\in Q^h, \tag{3.7}$$

where $\mathbf{M}_Q$ is a diagonal positive definite matrix. Its diagonal entry corresponding to point p is equal to V_{E_p}, the area of the dual zone E_p.

The second-order tensor $\mathbb{T}$ is represented by its tangential components $\mathbb{T}_e = \mathbb{T}\cdot\boldsymbol{\tau}_e$ on mesh edges, where $\boldsymbol{\tau}_e$ is the unit tangential vector to edge e. Let X^h be the space of such discrete tensors. The dimension of this space is twice the number of mesh edges. For $\mathbf{T}\in X^h$, we write $\mathbf{T}_e$ for the tangential component on mesh edge e, which is a two-dimensional vector. The boundary condition (3.6) implies that $\mathbf{T}_e\cdot\mathbf{n}_e = 0$ for every boundary edge e. The vector space X^h is equipped with the inner product:

$$[\mathbf{T},\,\mathbf{G}]_X \equiv (\mathbf{M}_X\mathbf{T})^T\,\mathbf{G}, \qquad \forall\mathbf{T},\mathbf{G}\in X^h, \tag{3.8}$$

where $\mathbf{M}_X$ is a symmetric positive definite matrix. Construction of this matrix is a non-trivial task since only tangential components of tensors are known.

Let edge e have end points p and p', and the tangential vector $\boldsymbol{\tau}_e$ point from p to p'. The mimetic gradient on edge e as an approximation of the directional derivative of the velocity:

$$\nabla\mathbf{u}\cdot\boldsymbol{\tau}_e \approx \frac{\mathbf{u}_{p'}-\mathbf{u}_p}{L_e} \equiv (\mathcal{GRAD}\,\mathbf{U})_e\,.$$

The mimetic divergence operator $\mathcal{DIV}_\mu$ is defined implicitly via the discrete Green formula:

$$[\mathbf{U},\,\mathcal{DIV}_\mu\mathbf{T}]_Q = -[\mathcal{GRAD}\,\mathbf{U},\,\mathbf{T}]_X, \qquad \forall\mathbf{U}\in Q^h,\,\mathbf{T}\in X^h, \tag{3.9}$$

which mimics the continuous formula:

$$\int_\Omega \mathbf{u} \cdot \operatorname{div}(\mu\mathbb{T})\,\mathrm{d}A = -\int_\Omega \nabla\,\mathbf{u} : (\mu\mathbb{T})\,\mathrm{d}A.$$

Note that the boundary conditions (3.6) were chosen to nullify the boundary integral in the Green formula. The continuous Green formula also implies that the inner product in the space of tensors is the weighted inner product and the weight is given by tensor μ. Using (3.7) and (3.8), we get that

$$\mathcal{DIV}_\mu = -\mathbf{M}_Q^{-1}\,\mathcal{GRAD}^{\,T}\,\mathbf{M}_X.$$

Since $\mathbf{M}_Q$ is the diagonal matrix, the divergence operator has a local stencil.

The inner product matrix $\mathbf{M}_X$ is the heart of the mimetic technology. Because we need to compute only $\mathcal{DIV}_\mu\,\mathcal{GRAD}$, the full matrix $\mathbf{M}_X$ is not needed. Using (3.5) and the discrete integration by parts formula (3.9), we get

$$(\mathbf{F}^{vis})^T\,\mathbf{V} = -[\mathcal{DIV}_\mu\,\mathcal{GRAD}\,\mathbf{U},\,\mathbf{V}]_Q = [\mathcal{GRAD}\,\mathbf{U},\,\mathcal{GRAD}\,\mathbf{V}]_X$$

for any vector $\mathbf{V}$. This argument shows that we need to define the inner product matrix $\mathbf{M}_X$ only on the space of discrete gradients, which is the subspace of X^h. In other words, we propose to calculate directly a stiffness matrix $\widetilde{\mathbf{M}}_X$ such that

$$[\mathcal{GRAD}\,\mathbf{U},\,\mathcal{GRAD}\,\mathbf{V}]_X \equiv (\widetilde{\mathbf{M}}_X\mathbf{U})^T\,\mathbf{V}, \qquad \forall \mathbf{U},\mathbf{V} \in Q^h, \tag{3.10}$$

where

$$\widetilde{\mathbf{M}}_X = \mathcal{GRAD}^{\,T}\,\mathbf{M}_X\,\mathcal{GRAD}\,. \tag{3.11}$$

Then,

$$\mathbf{F}^{vis} = \widetilde{\mathbf{M}}_X\,\mathbf{U}.$$

The conventional mimetic approach requires calculation of all terms in (3.11). However, since only the action of matrix $\mathbf{M}_X$ on subspace of discrete gradients is required for this, a faster calculation of $\widetilde{\mathbf{M}}_X$ is possible using the ideas described in [3].

For vector $\mathbf{V} \in X^h$, we denote its restriction to zone z by $\mathbf{V}_z$. The latter is composed of two dimensional vectors $\mathbf{v}_p$ (denoted also as $(\mathbf{V})_z^p$), where $p \in z$. Formula (3.10) represents the following integral:

$$(\widetilde{\mathbf{M}}_X\mathbf{U})^T\,\mathbf{V} = \int_\Omega \mu\,\nabla\mathbf{u}_h \colon \nabla\mathbf{v}_h\,\mathrm{d}A,$$

where $\mathbf{u}_h = \mathcal{L}(\mathbf{U})$ and $\mathbf{v}_h = \mathcal{L}(\mathbf{V})$. The additivity of integration implies that the calculation can be done zone-by-zone:

$$(\widetilde{\mathbf{M}}_X\mathbf{U})^T\mathbf{V} = \sum_{z\in\Omega_h} (\widetilde{\mathbf{M}}_z\mathbf{U}_z)^T\mathbf{V}_z, \qquad (\widetilde{\mathbf{M}}_z\mathbf{U}_z)^T\mathbf{V}_z = \int_z \mu_z\,\nabla\mathbf{u}_h \colon \nabla\mathbf{v}_h\,\mathrm{d}A, \tag{3.12}$$

where μ_z is a constant tensor approximating μ in zone z. This reduces calculation of the global matrix $\widetilde{\mathbf{M}}_X$ to calculation of smaller zonal matrices $\widetilde{\mathbf{M}}_z$. Still, the direct calculation of the integral in the right-hand side is not possible because value of the mesh functions

inside zone z depends on the reconstruction operators $\mathcal{L}$ which is not unique. We calculate the zonal matrix $\widetilde{\mathbf{M}}_z$ using general properties of the reconstruction operator rather than its precise form.

Let us formulate a few matrix equations for $\widetilde{\mathbf{M}}_z$ that mimics the Gauss-Green formulas. Consider a linear vector-function $\mathbf{u}_L$ and the corresponding vector of degrees of freedom $\mathbf{U}_L$. By the property of the reconstruction operator, $\mathbf{u}_L = \mathcal{L}(\mathbf{U}_L)$. Using the integration by parts, the reconstruction property stating that $\mathbf{v}_h$ is linear of mesh edges, and the trapezoidal quadrature rule for edge integrals, we get

$$\begin{aligned}\int_z \mu_z \nabla \mathbf{u}_L \colon \nabla \mathbf{v}_h \,\mathrm{d}A &= -\int_z \operatorname{div}(\mu_z \nabla \mathbf{u}_L) \cdot \mathbf{v}_h \,\mathrm{d}A + \int_{\partial z} (\mu_z \nabla \mathbf{u}_L \cdot \mathbf{n}_z) \cdot \mathbf{v}_h \,\mathrm{d}L \\ &= \int_{\partial z} (\mu_z \nabla \mathbf{u}_L \cdot \mathbf{n}_z) \cdot \mathbf{v}_h \,\mathrm{d}L = \sum_{e \in \partial z} (\mu_z \nabla \mathbf{u}_L \cdot \mathbf{n}_z^e) \cdot (\mathbf{v}_p + \mathbf{v}_{p'}) \frac{L_e}{2},\end{aligned}$$

where p and p' denote end points of edge e and are different in every term. The last sum can be rewritten as a dot product of a computable vector $\mathbf{R}_{L,z}$ and vector $\mathbf{V}_z$. Components of vector $\mathbf{R}_{L,z}$ depend of course on function $\mathbf{u}_L$ and tensor μ_z. Let e and e' be two edges of z meeting at point p. Then,

$$(\mathbf{R}_{L,z})^p = (\mu_z \nabla \mathbf{u}_L \cdot \mathbf{n}_z^e) \frac{L_e}{2} + (\mu_z \nabla \mathbf{u}_L \cdot \mathbf{n}_z^{e'}) \frac{L_{e'}}{2} = \mu_z \nabla \mathbf{u}_L \cdot \left(\mathbf{n}_z^e \frac{L_e}{2} + \mathbf{n}_z^{e'} \frac{L_{e'}}{2} \right). \tag{3.13}$$

Let $\mathbf{U}_{L,z}$ be the restriction of $\mathbf{U}_L$ to zone z. Combining the last three formulas, we get

$$(\widetilde{\mathbf{M}}_z \mathbf{U}_{L,z})^T \mathbf{V}_z = \mathbf{R}_{L,z}^T \mathbf{V}_z, \tag{3.14}$$

where $\mathbf{V}_z$ is an arbitrary vector. Now, we formulate the following problem: Find a symmetric matrix $\widetilde{\mathbf{M}}_z$ such that formula (3.14) is the identity for all linear functions $\mathbf{u}_L$. There are six linearly independent vector functions $\mathbf{u}_L$ that we denote by $\mathbf{b}_i$ (they form a basis in the space of linear vector functions):

$$\mathbf{b}_1 = \begin{bmatrix} x \\ 0 \end{bmatrix}, \quad \mathbf{b}_2 = \begin{bmatrix} y \\ 0 \end{bmatrix}, \quad \mathbf{b}_3 = \begin{bmatrix} 0 \\ x \end{bmatrix}, \quad \mathbf{b}_4 = \begin{bmatrix} 0 \\ y \end{bmatrix}, \quad \mathbf{b}_5 = \begin{bmatrix} 1 \\ 0 \end{bmatrix}, \quad \mathbf{b}_6 = \begin{bmatrix} 0 \\ 1 \end{bmatrix}.$$

Let $\mathbf{R}_{i,z}$ and $\mathbf{B}_{i,z}$ be the vectors from the right-hand and left-hand sides of (3.14), corresponding to vectors $\mathbf{R}_{L,z}$ and $\mathbf{U}_{L,z}$, respectively. Note that $\mathbf{R}_{5,z}$ and $\mathbf{R}_{6,z}$ are zero vectors, because the gradients of constant vectors $\mathbf{b}_5$ and $\mathbf{b}_6$ are zero tensors. Thus, we get four matrix equations:

$$\widetilde{\mathbf{M}}_z \mathbf{B}_{i,z} = \mathbf{R}_{i,z}, \qquad i = 1, 2, 3, 4. \tag{3.15}$$

To solve (3.15), we first calculate dot products

$$\alpha_{ij} = \mathbf{R}_{i,z}^T \mathbf{B}_{j,z} = \int_z \mu_z \nabla \mathbf{b}_i \colon \nabla \mathbf{b}_j \,\mathrm{d}A = (\mu_z \nabla \mathbf{b}_i \colon \nabla \mathbf{b}_j) A_z.$$

Let $\alpha = \{\alpha_{ij}\}_{i,j=1}^4$ be the square matrix of size four. This is the positive definite matrix for any positive definite tensor μ_z. Using definition of α^{-1}, we may verify that the matrix

$$\widetilde{\mathbf{M}}_z^{(0)} = \sum_{i,j=1}^4 (\alpha^{-1})_{ij} \mathbf{R}_{i,z} \mathbf{R}_{j,z}^T$$

satisfies equations (3.15). This is a semi-positive definite matrix. If we use these matrices to assemble the global matrix $\widetilde{\mathbf{M}}_X$, we get a semi-positive definite matrix with a huge null space. This matrix does not approximate the elliptic operator. Moreover, no artificial viscosity is added to the system when the velocity field lies in the null space. Thus, the zonal matrices must be corrected such that the assembled matrix becomes an approximation of the elliptic operator. More precisely, the null space of matrix $\widetilde{\mathbf{M}}_z$ may contain only constant vectors.

Let us define a subspace $\mathcal{U}_z$ of vectors orthogonal to six vectors $\mathbf{B}_{i,z}$. To correct the zonal matrix $\widetilde{\mathbf{M}}_z^{(0)}$, we add the orthogonal projector $\mathbf{P}_z$ onto $\mathcal{U}_z$:

$$\widetilde{\mathbf{M}}_z = \widetilde{\mathbf{M}}_z^{(0)} + \mathrm{trace}(\mu)\,\mathbf{P}_z, \tag{3.16}$$

where

$$\mathbf{P}_z^2 = \mathbf{P}_z = \mathbf{P}_z^T, \qquad \mathbf{P}_z\,\mathbf{B}_{i,z} = 0, \qquad i = 1,\ldots,6. \tag{3.17}$$

By construction, the resulting matrix satisfies equations (3.15). Calculation of the orthogonal projector is a well studied linear algebra problem. Let us form a matrix $\mathbf{B}_z$ with six columns $\mathbf{B}_{i,z}$. Then, the orthogonal projector is given by

$$\mathbf{P}_z = \mathbf{I}_z - \mathbf{B}_z\,(\mathbf{B}_z^T\,\mathbf{B}_z)^{-1}\,\mathbf{B}_z^T,$$

where $\mathbf{I}_z$ is the identity matrix of the same size as $\mathbf{P}_z$. This completes the derivation of the local stiffness matrix. The calculation of vector $\mathbf{F}^{vis}$ reduces now to calculation of local matrix-vector products $\mathbf{F}_z^{vis} = \widetilde{\mathbf{M}}_z\,\mathbf{U}_z$. The two-dimensional vector $(\mathbf{F}_z^{vis})^p$ is the subzonal viscous point force $(\mathbf{f}^{vis})_z^p$ needed in (3.4).

3.3 A case of scalar viscosity coefficient

The tensor form of the viscosity coefficient μ opens doors for building various methods that will be studied in a separate paper. Here we focus on a simpler model where μ is a scalar. In this case, the matrix α is diagonal with equal diagonal entries, $\alpha = \mu_z\,A_z\,\mathbf{I}$. Formula (3.16) reduces to

$$\widetilde{\mathbf{M}}_z = \frac{1}{\mu_z\,A_z}\sum_{i=1}^{4}\mathbf{R}_{i,z}\,\mathbf{R}_{i,z}^T + \mu_z\,\mathbf{P}_z. \tag{3.18}$$

To study this matrix in more detail, we split it into four square matrices. We collect the first components of two-dimensional vectors $(\mathbf{R}_{i,z})^p$ into one group and the other components into the second group. To simplify notation, the vectors with reordered components are still denoted by $\mathbf{R}_{i,z}$. We perform the same reordering of components for vectors $\mathbf{B}_{i,z}$:

$$\mathbf{R}_{i,z} = \begin{bmatrix} \mathbf{R}_{i,z}^{(x)} \\ \mathbf{R}_{i,z}^{(y)} \end{bmatrix}, \qquad \mathbf{B}_{i,z} = \begin{bmatrix} \mathbf{B}_{i,z}^{(x)} \\ \mathbf{B}_{i,z}^{(y)} \end{bmatrix}.$$

Definition (3.13) implies that

$$\mathbf{R}_{1,z}^{(y)} = \mathbf{R}_{2,z}^{(y)} = \mathbf{R}_{5,z}^{(y)} = 0 \qquad \text{and} \qquad \mathbf{R}_{3,z}^{(x)} = \mathbf{R}_{4,z}^{(x)} = \mathbf{R}_{6,z}^{(x)} = 0.$$

Similar identities hold for subvectors $\mathbf{B}_{i,z}^{(x)}$ and $\mathbf{B}_{i,z}^{(y)}$. Using these identities in (3.18) and (3.17), we conclude that both the matrix $\widetilde{\mathbf{M}}_z$ and the projector $\mathbf{P}_z$ are block-diagonal matrices with two blocks corresponding to two velocity components:

$$\widetilde{\mathbf{M}}_z = \begin{bmatrix} \widetilde{\mathbf{M}}_z^{(x)} & 0 \\ 0 & \widetilde{\mathbf{M}}_z^{(y)} \end{bmatrix}, \qquad \mathbf{P}_z = \begin{bmatrix} \mathbf{P}_z^{(x)} & 0 \\ 0 & \mathbf{P}_z^{(y)} \end{bmatrix}, \tag{3.19}$$

where matrices $\widetilde{\mathbf{M}}_z^{(x)}$ and $\widetilde{\mathbf{M}}_z^{(y)}$ can be written in the form similar to (3.18). For instance,

$$\widetilde{\mathbf{M}}_z^{(x)} = \frac{1}{\mu_z A_z} \sum_{i=1}^{2} \mathbf{R}_{i,z}^{(x)} \, (\mathbf{R}_{i,z}^{(x)})^T + \mu_z \, \mathbf{P}_z^{(x)}, \tag{3.20}$$

where $\mathbf{P}_z^{(x)}$ is the orthogonal projector such that

$$(\mathbf{P}_z^{(x)})^2 = \mathbf{P}_z^{(x)}, \qquad \mathbf{P}_z^{(x)} \, \mathbf{B}_{i,z}^{(x)} = 0, \qquad i = 1, 2, 5. \tag{3.21}$$

Let us form a matrix $\mathbf{B}_z^{(x)}$ with three columns $\mathbf{B}_{i,z}^{(x)}$, $i = 1, 2, 5$. Then, the orthogonal projector is given by (compare with the formula for $\mathbf{P}_z$):

$$\mathbf{P}_z^{(x)} = \mathbf{I}_z^{(x)} - \mathbf{B}_z^{(x)} \left((\mathbf{B}_z^{(x)})^T \, \mathbf{B}_z^{(x)} \right)^{-1} (\mathbf{B}_z^{(x)})^T.$$

Observe that additional relationships hold by construction:

$$\mathbf{R}_{1,z}^{(x)} = \mathbf{R}_{3,z}^{(y)}, \qquad \mathbf{R}_{2,z}^{(x)} = \mathbf{R}_{4,z}^{(y)} \qquad \text{and} \qquad \mathbf{R}_{5,z}^{(x)} = \mathbf{R}_{6,z}^{(y)}.$$

Similar relationships hold for subvectors $\mathbf{B}_{i,z}^{(x)}$ and $\mathbf{B}_{i,z}^{(y)}$. This implies that both blocks in (3.19) are identical. The global matrix $\widetilde{\mathbf{M}}_X$ is assembled from zonal matrices $\widetilde{\mathbf{M}}_z$; therefore, it remains block-diagonal with two equal blocks that are approximations of the scalar elliptic operator $-\mathrm{div}\,(\mu \nabla\,)$.

3.4 Viscosity coefficient

In this paper, we use expression for the viscosity coefficient described in [30]:

$$\mu_z = \psi_z \, \rho_z \, L_z \left(c_Q \frac{\gamma - 1}{4} |\Delta \mathbf{u}| + \sqrt{c_Q^2 \left(\frac{\gamma - 1}{4} \right)^2 |\Delta \mathbf{u}|^2 + c_L^2 s_z^2} \right),$$

where s_z is the zonal sound speed, c_L and c_Q are positive non-dimensional constants, L_z is the characteristic length, $\Delta \mathbf{u}$ is the measure of compressibility (a scalar, for instance, the velocity jump across the shock), and ψ_z is a binary switch.

The binary switch ensures that the heating due to artificial viscosity occurs only for zones under compression. In numerical experiments, we set $\psi_z = 1$ when $\Delta \mathbf{u} > 0$ and $\psi_z = 0$ otherwise. The measure of compression is defined as follows:

$$\Delta \mathbf{u} = \frac{L_z}{A_z} \int_{\partial z} \mathbf{u}_h \cdot \mathbf{n}_z \, \mathrm{d}L.$$

In the numerical experiments, we set $c_L = c_Q = 1$. We use two simple estimates for the characteristic length L_z. The first estimate uses $L_z = L_z^a$, where $L_z^a = \sqrt{A_z}$, and is appropriate for meshes with mild variation in areas of neighboring zones. The second estimate defines $L_z = L_z^u$, where L_z^u is the zone size in the direction of average momentum. To reduce variations of L_z^u on unstructured meshes, we smooth the calculated characteristic length using 2-3 Jacoby iterations:

$$L_z^{u,k+1} = \frac{1}{2} L_z^{u,k} + \frac{1}{2\,K_z} \sum_{z'} L_{z'}^{u,k}, \qquad k \geq 0,$$

where K_z is the number of closest neighbors z' of zone z. Development of robust models for the viscosity coefficient on unstructured meshes is the topic of active research but beyond the scope of this article.

4 The $r - z$ coordinate system

In the r-z coordinate system, a continuous non-conservative form of the momentum equation divided by r looks exactly as the momentum equation in the x-y coordinate system [2]. Essentially all discrete symmetry preserving methods in $r - z$ exploit this fact and use the Cartesian form of the momentum equation:

$$\langle \rho_h A \rangle_p \, \frac{D\mathbf{u}_p}{Dt} = \sum_{z \ni p} \mathbf{f}_z^p, \qquad \widetilde{m}_z \frac{D\varepsilon_z}{Dt} = -\sum_{p \in z} r_p \, \mathbf{f}_z^p \cdot \mathbf{u}_p, \tag{4.22}$$

where $\widetilde{m}_z$ is the true zonal mass and $\langle \rho_h A \rangle_p$ is a specially defined 'Cartesian' mass of point p. Let V_z be the volume of zone z and m_z^p be a subzonal mass associated with point p of zone z. The subzonal mass is independent of time. The detailed analysis presented in [2] gives

$$\widetilde{m}_z = \sum_{p \in z} \tilde{m}_z^p, \qquad \widetilde{m}_p = \sum_{z \ni p} \tilde{m}_z^p, \qquad \tilde{m}_z^p = r_p \, \rho_z^p \, A_z^p,$$

and

$$\langle \rho_h A \rangle_p = \sum_{z \ni p} \rho_z^p \, A_z^p,$$

Here A_z^p are nothing else but positive quadrature weights in the formula for volume,

$$V_z = \int_z r \, \mathrm{d}r \, \mathrm{d}z = \sum_{p \in z} r_p \, A_z^p,$$

and ρ_z^p is the subzonal density that is calculated from the formula for the subzonal mass $\tilde{m}_p^z$ when $r_p \neq 0$. For points lying on the z-axis, the subzonal densities have to be defined from other principles. One of the principles used in Section 5 is the symmetry preservation on 'polar' meshes. The authors of [2] suggest to take values for such ρ_z^p from the closest $p' \in z$ with $r_{p'} \neq 0$. On a general polygonal mesh, where two neighboring points satisfy this criterion, the point with the smallest $r_{p'}$ is chosen. Note that the quadrature weights A_z^p are not unique but must comply with the symmetry preservation principle.

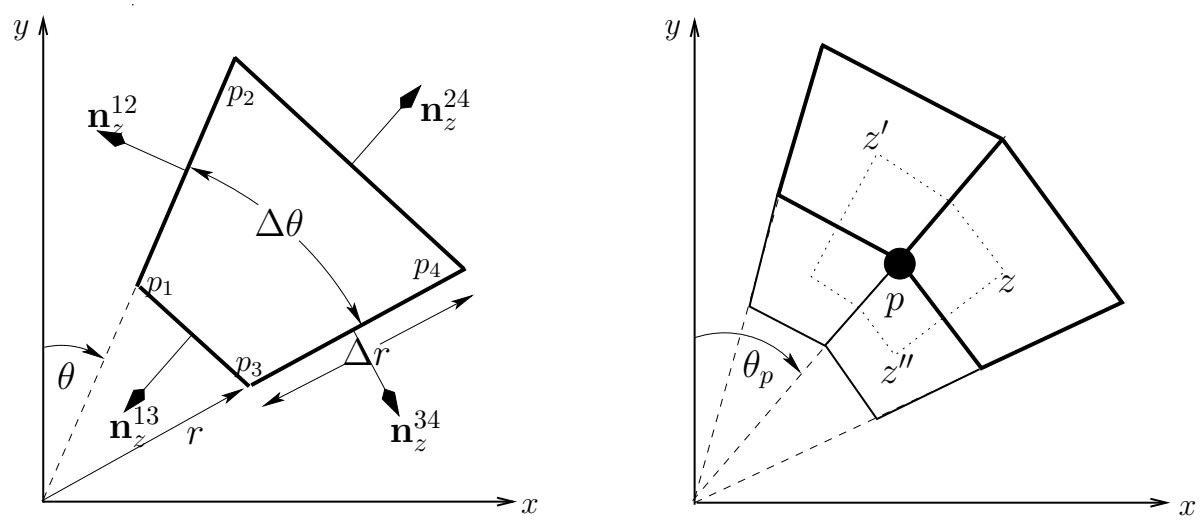

Figure 1: Left picture: A quadrilateral zone z. Right picture: Solid lines show four quadrilateral zones sharing a common point p. Dashed lines mark the dual zone E_p.

5 Symmetry analysis

In this section, we analyze how the staggered discretization preserves the cylindrical symmetry in the x-y coordinate system and spherical symmetry in the r-z coordinate system on meshes obtained by connecting points of true polar meshes by straight lines. One of the resulting quadrilateral elements is shown in Fig. 1. We assume that the polar mesh is uniform in the angular direction, $\Delta\theta = constant$.

Here we focus only on symmetry of operators and forces assuming implicitly that the boundary and initial conditions, and the viscosity model for μ_z respect the symmetry.

5.1 Cylindrical symmetry of pressure forces

Cylindrical symmetry requires the pressure and the internal energy be functions of only radius $r = \sqrt{x^2 + y^2}$ and the velocity vector be oriented along the radius vector:

$$\mathrm{p} = \mathrm{p}(r), \quad \varepsilon = \varepsilon(r), \quad \mathbf{u} = u(r)\,(\sin\theta,\, \cos\theta)^T, \tag{5.1}$$

where θ is the polar angle. We assume that $\theta = 0$ corresponds to the direction of the y-axis. For discrete functions, relaxed symmetry requirements are more appropriate:

$$\mathrm{p}_h = \mathrm{p}_h(r, \Delta\theta), \quad \varepsilon_h = \varepsilon_h(r, \Delta\theta), \quad \mathbf{u}_h = u_h(r, \Delta\theta)\,(\sin\theta,\, \cos\theta)^T. \tag{5.2}$$

We shall also highlight special cases when the discrete functions do not depend on $\Delta\theta$.

Let us consider the quadrilateral zone z shown in Fig. 1. Let $(r_p,\, \theta_p)$ be the polar coordinates of point p. As shown in this figure, $p_1 = p$.

The analysis of symmetry is focused on a 'polar' layer with the interior radius r_p and the exterior radius $r_p + \Delta r$. Note that Δr is considered as a function of r_p. The pressure,

density, internal energy, and the viscosity coefficient μ are assumed to be constant in this layer. The velocity field is assumed to have constant amplitude on the interior and exterior boundaries. Our goal is to show that the subzonal forces in (3.2) preserve this symmetry. We shall use superscript 'ref' for vectors and matrices that depend only on r_p and $\Delta\theta$.

Let us introduce the matrix $\mathcal{R}_\theta$,

$$\mathcal{R}_\theta = \begin{bmatrix} \cos\theta & \sin\theta \\ -\sin\theta & \cos\theta \end{bmatrix},$$

which describes clockwise rotation in the x-y plane on angle θ. It will be convenient to use two superscripts to represent edge length L_z^{ij} and the corresponding normal vector $\mathbf{n}_z^{ij}$. Then,

$$\mathbf{n}_z^{24} = \mathcal{R}_{\theta_p+\Delta\theta/2} \begin{bmatrix} 0 \\ 1 \end{bmatrix}, \quad \mathbf{n}_z^{12} = \mathcal{R}_{\theta_p+\Delta\theta/2} \begin{bmatrix} -\cos(\Delta\theta/2) \\ -\sin(\Delta\theta/2) \end{bmatrix}, \quad \mathbf{n}_z^{34} = \mathcal{R}_{\theta_p+\Delta\theta/2} \begin{bmatrix} \cos(\Delta\theta/2) \\ -\sin(\Delta\theta/2) \end{bmatrix},$$

and $\mathbf{n}_z^{13} = -\mathbf{n}_z^{24}$. We also need the following formulas:

$$A_z = (r_p + \Delta r/2)\,\Delta r\,\sin\Delta\theta, \qquad L_z^{13} = 2\,r_p \sin(\Delta\theta/2), \qquad L_z^{12} = \Delta r. \tag{5.3}$$

Definition of the subzonal pressure point force (3.3) gives

$$(\mathbf{f}^{prs})_z^p = \frac{\mathrm{p}_z}{2}\left(\mathbf{n}_z^{13} L_z^{13} + \mathbf{n}_z^{12} L_z^{12}\right).$$

Four subzonal forces will contribute to the force acting at point p (see the right picture in Fig. 1). This summation of subzonal forces can be done in pairs that belong to the same 'polar' layer. Let us consider the pair z and z' shown on the right picture in Fig. 1. By assumption $\mathrm{p}_z = \mathrm{p}_{z'}$. From geometry, we conclude that $L_z^{13} = L_{z'}^{13}$ and $\mathbf{n}_z^{12} = -\mathbf{n}_{z'}^{34}$. Thus,

$$(\mathbf{f}^{prs})_z^p + (\mathbf{f}^{prs})_{z'}^p = \frac{\mathrm{p}_z}{2} L_z^{13}\left(\mathbf{n}_z^{13} + \mathbf{n}_{z'}^{13}\right) = -\mathrm{p}_z\, r_p\, \sin(\Delta\theta)\, \mathcal{R}_{\theta_p} \begin{bmatrix} 0 \\ 1 \end{bmatrix}.$$

The right-hand is the clockwise rotation of a reference force vector by angle θ_p. A similar argument can be applied to the other pair of zones around point p. Summation of these forces will give the pressure point force:

$$(\mathbf{f}^{prs})^p = \mathcal{R}_{\theta_p}\,(\mathbf{f}_{ref}^{prs})^p, \qquad (\mathbf{f}_{ref}^{prs})^p = -(\mathrm{p}_z - \mathrm{p}_{z''})\, r_p\, \sin(\Delta\theta) \begin{bmatrix} 0 \\ 1 \end{bmatrix}. \tag{5.4}$$

Remark 5.1 *Comparing (5.4) with the formula (5.3) for area A_z, we observe the same dependence on the polar angle $\Delta\theta$. Since the point mass m_p is proportional to A_z, the discrete momentum equation (3.2), in absence of artificial viscous forces, becomes the one-dimensional equation.*

Analysis of energy equation requires to write subzonal forces in a form similar to (5.4):

$$(\mathbf{f}^{prs})_z^p = \mathcal{R}_{\theta_p}\,(\mathbf{f}_{ref}^{prs})_z^p. \tag{5.5}$$

Direct calculations give

$$(\mathbf{f}_{ref}^{prs})_z^{p_1} = \frac{\mathrm{p}_z}{2}\begin{bmatrix} -2\,r_{p_1}\,\sin^2(\Delta\theta/2) - \Delta r \\ -r_{p_1}\,\sin(\Delta\theta) \end{bmatrix}, \quad (\mathbf{f}_{ref}^{prs})_z^{p_2} = \frac{\mathrm{p}_z}{2}\begin{bmatrix} 2\,r_{p_2}\,\sin^2(\Delta\theta/2) - \Delta r \\ r_{p_2}\,\sin(\Delta\theta) \end{bmatrix} \quad (5.6)$$

for points p_1 and p_2, and

$$(\mathbf{f}_{ref}^{prs})_z^{p_3} = \frac{\mathrm{p}_z}{2}\begin{bmatrix} 2\,r_{p_3}\,\sin^2(\Delta\theta/2) + \Delta r \\ -r_{p_3}\,\sin(\Delta\theta) \end{bmatrix}, \quad (\mathbf{f}_{ref}^{prs})_z^{p_4} = \frac{\mathrm{p}_z}{2}\begin{bmatrix} -2\,r_{p_4}\,\sin^2(\Delta\theta/2) + \Delta r \\ r_{p_4}\,\sin(\Delta\theta) \end{bmatrix}. \quad (5.7)$$

for points p_3 and p_4. Recall that Δr is the function of r_{p_1}.

5.2 Cylindrical symmetry of artificial viscous forces

Let us show that the artificial viscous force also preserves cylindrical symmetry on the 'polar' mesh. The analysis is focused again on one 'polar' layer. Recall that the vector of subzonal forces is $\mathbf{F}_z^{vis} = \widetilde{\mathbf{M}}_z\mathbf{U}_z$ and subzonal point force is $(\mathbf{F}_z^{vis})^p$. We omit superscript 'vis' for the rest of this subsection.

The block-diagonal structure of $\widetilde{\mathbf{M}}_z$ allows us to analyze each velocity component independently; however, analysis becomes shorter when applied simultaneously to subvectors $\mathbf{U}_z^{(x)}$ and $\mathbf{U}_z^{(y)}$. For the quadrilateral element z shown on the left picture in Fig. 1, these subvectors have four components.

In a finite element method, the integral in (3.12) is invariant with respect to rotation and gives the same stiffness matrix for each zone in the 'polar' layer. This simplifies the analysis of symmetry. In the MFD method, construction of the stiffness matrix is pure algebraic. To follow the finite element path, additional non-trivial properties of the lifting operator must be proved including also its existence. Therefore, we employ another technique for the symmetry analysis.

Using the local ordering of vertexes shown in Fig. 1, we define two subspaces of $\Re^4$:

$$\mathcal{S}^+ = \{\mathbf{V} = (a,\,b,\,a,\,b)^T, \quad a, b \in \Re^1\}, \qquad \mathcal{S}^- = \{\mathbf{V} = (a,\,b,\,-a,\,-b)^T, \quad a, b \in \Re^1\}.$$

The following result is proved immediately by observing that spaces $\mathcal{S}^+$ and $\mathcal{S}^-$ are orthogonal to each other.

Lemma 5.1 *For any number of vectors $\mathbf{V}_1, \ldots, \mathbf{V}_k$ from space $\mathcal{S} = \mathcal{S}^+ \cup \mathcal{S}^-$ and the matrix $\mathbf{H} = \sum_{i=1}^k \mathbf{V}_i\mathbf{V}_i^T$, we get the following inclusions:*

$$\mathbf{H}\,\mathbf{W} \in \mathcal{S}^+ \ (\textit{resp.}, \ \mathcal{S}^-) \qquad \textit{when} \qquad \mathbf{W} \in \mathcal{S}^+ \ (\textit{resp.}, \ \mathcal{S}^-).$$

Let us show that matrix $\widetilde{\mathbf{M}}_z$ has the form needed for the above lemma. We start with writing the first term of (3.20) as the product of two 4×2 matrices:

$$\sum_{i=1}^{2} \mathbf{R}_{i,z}^{(x)}\,(\mathbf{R}_{i,z}^{(x)})^T = \left[\mathbf{R}_{1,z}^{(x)};\ \mathbf{R}_{2,z}^{(x)}\right]\,\left[\mathbf{R}_{1,z}^{(x)};\ \mathbf{R}_{2,z}^{(x)}\right]^T,$$

where $[\mathbf{a};\mathbf{b}]$ denotes a matrix with two columns $\mathbf{a}$ and $\mathbf{b}$. To simplify notation, we define $\mathrm{c} = \cos(\Delta\theta/2)$ and $\mathrm{s} = \sin(\Delta\theta/2)$. Using formula (3.13) and formulas for normal vectors, we get

$$\left[\mathbf{R}_{1,z}^{(x)};\ \mathbf{R}_{2,z}^{(x)}\right] = \frac{\mu_z}{2}\begin{bmatrix} L_z^{12}\,(\mathbf{n}_z^{12})^T + L_z^{13}\,(\mathbf{n}_z^{13})^T \\ L_z^{24}\,(\mathbf{n}_z^{24})^T + L_z^{12}\,(\mathbf{n}_z^{12})^T \\ L_z^{13}\,(\mathbf{n}_z^{13})^T + L_z^{34}\,(\mathbf{n}_z^{34})^T \\ L_z^{34}\,(\mathbf{n}_z^{34})^T + L_z^{24}\,(\mathbf{n}_z^{24})^T \end{bmatrix} = \frac{\mu_z}{2}\begin{bmatrix} -\mathrm{c}\,L_z^{12} & -\mathrm{s}L_z^{12} - L_z^{13} \\ -\mathrm{c}\,L_z^{12} & -\mathrm{s}L_z^{12} + L_z^{24} \\ \mathrm{c}\,L_z^{34} & -\mathrm{s}L_z^{34} - L_z^{13} \\ \mathrm{c}\,L_z^{34} & -\mathrm{s}L_z^{34} + L_z^{24} \end{bmatrix} \mathcal{R}_{\theta_p+\Delta\theta/2}^T.$$

Both columns in the last matrix depend only on r, Δr, and $\Delta\theta$. Thus,

$$\left[\mathbf{R}_{1,z}^{(x)};\ \mathbf{R}_{2,z}^{(x)}\right] = \left[\mathbf{R}_{1,z}^{(x),ref};\ \mathbf{R}_{2,z}^{(x),ref}\right]\mathcal{R}_{\theta_p+\Delta\theta/2}^T, \qquad \mathbf{R}_{1,z}^{(x),ref} \in \mathcal{S}^-, \quad \mathbf{R}_{2,z}^{(x),ref} \in \mathcal{S}^+.$$

Since $\mathcal{R}_\theta^T\mathcal{R}_\theta$ is the identity matrix for any angle θ, we conclude that the first term in zonal matrix $\widetilde{\mathbf{M}}_z$ depends only on the cylindrical radius r_p and $\Delta\theta$.

Straightforward calculations show that the following matrix is the orthogonal projector satisfying properties (3.21):

$$\mathbf{P}_z = \frac{1}{\|\mathbf{N}_z^{(x)}\|^2}\,\mathbf{N}_z^{(x)}\,(\mathbf{N}_z^{(x)})^T, \qquad \mathbf{N}_z^{(x)} = (r+\Delta r;\ -r;\ -r-\Delta r;\ r)^T \in \mathcal{S}^-.$$

This implies that the second term in the zonal matrix $\widetilde{\mathbf{M}}_z$ depends only on r and $\Delta\theta$. Therefore, we can add superscript 'ref' to it, $\widetilde{\mathbf{M}}_z = \widetilde{\mathbf{M}}_z^{ref}$. Moreover, the matrix $\widetilde{\mathbf{M}}_z^{ref}$ has the form required for applying Lemma 5.1.

Assumption of the cylindrical symmetry (5.1) for the velocity vector gives

$$\mathbf{u}_p = \mathcal{R}_{\theta_p}(\mathbf{u}^{ref})^p, \qquad (\mathbf{u}^{ref})^p = \begin{bmatrix} 0 \\ u(r_p) \end{bmatrix}. \tag{5.8}$$

Applying this formula to four vertices of zone z, we get

$$\mathbf{U}_z^{(x)} = \begin{bmatrix} u(r_p)\,\sin\theta_p \\ u(r_p+\Delta r)\,\sin\theta_p \\ u(r_p)\,\sin(\theta_p+\Delta\theta) \\ u(r_p+\Delta r)\,\sin(\theta_p+\Delta\theta) \end{bmatrix}, \qquad \mathbf{U}_z^{(y)} = \begin{bmatrix} u(r_p)\,\cos\theta_p \\ u(r_p+\Delta r)\,\cos\theta_p \\ u(r_p)\,\cos(\theta_p+\Delta\theta) \\ u(r_p+\Delta r)\,\cos(\theta_p+\Delta\theta) \end{bmatrix}.$$

The argument is not changed if we consider assumptions (5.2). Selecting the part independent of θ, we get

$$[\mathbf{U}_z^{(x)};\ \mathbf{U}_z^{(y)}] = [\mathbf{U}_z^{(x),ref};\ \mathbf{U}_z^{(y),ref}]\,\mathcal{R}_{\theta_p+\Delta\theta/2}^T, \qquad \mathbf{U}_z^{(x),ref} \in \mathcal{S}^-, \quad \mathbf{U}_z^{(y),ref} \in \mathcal{S}^+.$$

Summarizing, for every cylindrical layer, the matrix $[\mathbf{F}^{(x)};\,\mathbf{F}^{(y)}]$ is the product of a reference stiffness matrix, the reference 4×2 matrix and the rotation matrix. The Lemma 5.1 gives that

$$[\mathbf{F}_z^{(x)};\ \mathbf{F}_z^{(y)}] = [\mathbf{F}_z^{(x),ref};\ \mathbf{F}_z^{(y),ref}]\,\mathcal{R}_{\theta_p+\Delta\theta/2}^T, \qquad \mathbf{F}_z^{(x),ref} \in \mathcal{S}^-, \quad \mathbf{F}_z^{(y),ref} \in \mathcal{S}^+. \tag{5.9}$$

Every row of the reference 4×2 matrix is the subzonal viscous point force. Definition of spaces $\mathcal{S}^+$ and $\mathcal{S}^-$ implies that the reference subzonal force at point p_1 (see the left picture in Fig. 2) is the mirror image of the references subzonal force at point p_3 with respect to the y-axis. The same is true for the other pair of points.

Formula (5.9) states that the actual force is obtained by rotation of the reference force by angle $\theta_p + \Delta\theta/2$. The right picture in Fig. 2 is the geometric proof of the fact that the sum of two subzonal viscous forces at point p acts along the diagonal of the parallelogram attached to point p. Since these forces are equal and mirror images of one another with respect to line passing through the origin and point p, this direction is radial.

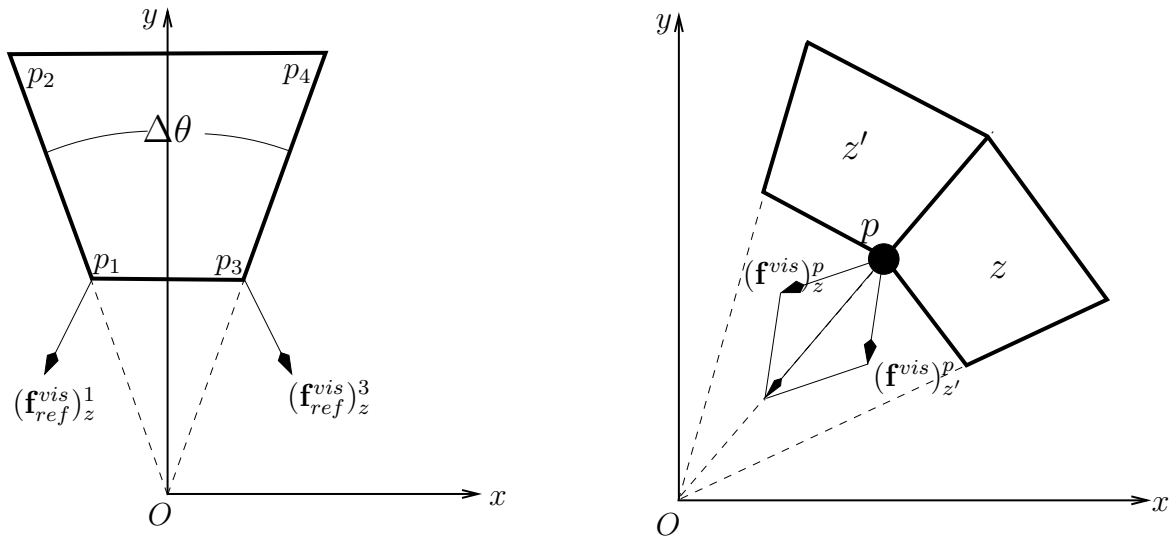

Figure 2: Left picture: subzonal forces for a reference zone. Right picture: summation of subzonal forces at point p

Repeating the above argument for the other pair of zones around point p, we conclude, that the total viscous point force can be written as follows:

$$(\mathbf{f}^{vis})^p = \mathcal{R}_{\theta_p}\,(\mathbf{f}^{vis}_{ref})^p, \qquad (\mathbf{f}^{vis}_{ref})^p = \begin{bmatrix} 0 \\ (f^{vis}_{ref})^p \end{bmatrix}, \tag{5.10}$$

where $(r_p,\, \theta_p)$ are the polar coordinates of point p, and the reference force $(f^{vis}_{ref})^p$ depends only on r_p and $\Delta\theta$.

Remark 5.2 *Detailed formula for $(f^{vis}_{ref})^p$ shows non-trivial dependence on $\Delta\theta$ and the one-dimensional momentum equations are obtained only in the limit $\Delta\theta \to 0$. Allowing μ_z to be the full tensor could be a possible way for eliminating dependence on $\Delta\theta$.*

Analysis of energy equation requires to write subzonal forces in a form similar to (5.10):

$$(\mathbf{f}^{vis})^p_z = \mathcal{R}_{\theta_p}\,(\mathbf{f}^{vis}_{ref})^p_z. \tag{5.11}$$

The reference subzonal forces $(\mathbf{f}^{vis}_{ref})^p_z$ follow from rotation of reference forces in (5.9) by angle $\pm\Delta\theta/2$. For instance, taking the first and the third rows in the reference matrix to form two-dimensional vectors $(\mathbf{F}^{ref}_z)^{p_1}$ and $(\mathbf{F}^{ref}_z)^{p_3}$, respectively, and noting that $\mathcal{R}_\theta\mathcal{R}_{\theta'} = \mathcal{R}_{\theta+\theta'}$, we get

$$(\mathbf{f}^{vis}_{ref})^{p_1}_z = \mathcal{R}_{-\Delta\theta/2}(\mathbf{F}^{ref}_z)^{p_1}, \qquad (\mathbf{f}^{vis}_{ref})^{p_3}_z = \mathcal{R}_{\Delta\theta/2}(\mathbf{F}^{ref}_z)^{p_3} \tag{5.12}$$

for points p_1 and p_3.

5.2.1 Triangles at the origin

At the origin, quadrilateral zones become triangular zones. On a triangular zone, the MFD method reduces to the linear finite element method. Indeed, the orthogonal projector $\mathbf{P}^{(x)}_z$ should be a 3×3 matrix satisfying conditions (3.21). Since vectors $\mathbf{B}^{(x)}_{1,z}$, $\mathbf{B}^{(x)}_{2,z}$ and $\mathbf{B}^{(x)}_{5,z}$ are linearly independent, this is possible only when the projector is the zero matrix; therefore, the stiffness matrix (3.20) is fully defined by two functions x and y.

The mesh function $\mathbf{u}_h$ is always linear on a triangle; therefore, the integral representation (3.12) can be used for analysis of symmetry. This integral is independent with respect to rotation of triangle z. It is easy to verify that on the reference triangle (the dashed triangle $O\,p_1\,p_3$ on the left picture in Fig. 2), two subzonal point forces (at points other than the origin) will be mirror images of one another.

5.2.2 Subzonal forces for boundary points

The impermeable boundary condition, $\mathbf{u}\cdot\mathbf{n} = 0$, allows us to reflect the mesh and the velocity field about radial boundaries ($\theta = const$). After that, the boundary point can be treated as an internal point and the above arguments can be applied.

More efficient implementation is based of the observation that the mass of a boundary point is twice less than the mass of an internal point with the same radius. Thus, the equivalent approach is to split the point force $\mathbf{f}^p$ into normal to boundary and tangential components and set the latter to zero.

5.3 Spherical symmetry of subzonal forces

Spherical symmetry requires pressure and internal energy be functions of only radius $R = \sqrt{r^2 + z^2}$ and the velocity vector be oriented along the radius vector, i.e. they have again the form (5.1). For mesh calculations, relaxed assumptions of the spherical symmetry, similar to (5.2), are more appropriate.

In the r-z coordinate system, analysis of the right-hand side of the momentum equation (4.22) proceeds as is Section 5.1. Let $(R_p,\, \theta_p)$ be the polar coordinate of point p. We assume that the pressure, density, internal energy, and the viscosity coefficient μ are constant in each 'polar' layer. We also assume that the velocity field has constant amplitude on the interior and exterior boundaries of this layer. The goal is to show that the subzonal forces in (4.22) preserve this symmetry.

A novel step in the analysis is to show that $\langle \rho_h A \rangle_p$ in the left-hand side is independent of θ. This is true when the quadrature weights A^p_z are independent of θ. To apply arguments

from subsection 5.2.2, we need to distribute these weights symmetrically (see Fig. 1):

$$A_z^{p_1} = A_z^{p_3} \qquad \text{and} \qquad A_z^{p_2} = A_z^{p_4}.$$

For the 'polar' mesh considered in this section, a solution proposed in [2] gives:

$$A_z^{p_1} = \sin(\Delta\theta)\,\Delta R\,(R_{p_1} + \frac{1}{3}\Delta R) \qquad \text{and} \qquad A_z^{p_2} = \sin(\Delta\theta)\,\Delta R\,(R_{p_2} + \frac{2}{3}\Delta R).$$

Note that this solution is not unique. Comparing with formula (5.3), we observe that angular dependence of $\langle \rho_h A \rangle_p$ is in the same form. This implies that in absence of artificial viscosity forces $\sin(\Delta\theta)$ will cancel out in the momentum equation giving the one-dimensional discrete equations. Otherwise, we have the spherically symmetric solution that depends on R and $\Delta\theta$.

5.4 Analysis of energy equation

We begin with analysis of the cylindrical symmetry in the x-y coordinate system. Let us consider again the cells z shown in Fig. 1 and the second equation in (3.2). Since the force vectors (5.5) and (5.11), and the velocity vectors (5.8) are obtained by rotation of the reference vectors, we get

$$m_z \frac{D\varepsilon_z}{Dt} = -\sum_{p\in z} \mathbf{f}_z^p \cdot \mathbf{u}_p = -\sum_{p\in z} \left[(\mathbf{f}_{ref}^{prs})_z^p \cdot (\mathbf{u}^{ref})^p + (\mathbf{f}_{ref}^{vis})_z^p \cdot (\mathbf{u}^{ref})^p \right]. \tag{5.13}$$

Since m_z is constant in a considered layer, the discrete internal energy preserves the cylindrical symmetry; however, it depends on $\Delta\theta$. In the absence of artificial viscous forces, a stronger result can be shown. According to (5.3), the zonal mass has factor $\sin(\Delta\theta)$. Using formulas (5.6),(5.7) and (5.8), we get

$$\sum_{p\in z} (\mathbf{f}_{ref}^{prs})_z^p \cdot (\mathbf{u}^{ref})^p = \mathrm{p}_z\, \sin(\Delta\theta)\,(r_{p_2}\, u(r_{p_2}) - r_{p_1}\, u(r_{p_1})).$$

Thus, the factor $\sin(\Delta\theta)$ is canceled in both sides of the energy equation giving the one-dimensional equations.

We continue with analysis of the spherical symmetry in the r-z coordinate system. Applying the above argument to the second equation in (4.22), it can be rewritten as follows:

$$\tilde{m}_z \frac{D\varepsilon_z}{Dt} = -\sum_{p\in z} r_p\, \mathbf{f}_z^p \cdot \mathbf{u}_p = -\sum_{p\in z} r_p\, \left((\mathbf{f}_{ref}^{prs})_z^p \cdot (\mathbf{u}^{ref})^p + (\mathbf{f}_{ref}^{vis})_z^p \cdot (\mathbf{u}^{ref})^p \right). \tag{5.14}$$

Using first formulas (5.6), (5.7) and (5.8) (with R_p in place of r_p), and then inserting r-coordinates of points, we obtain

$$\begin{aligned} \sum_{p\in z} r_p\, (\mathbf{f}_{ref}^{prs})_z^p \cdot (\mathbf{u}^{ref})^p &= \frac{\mathrm{p}_z}{2} \sin(\Delta\theta)\, [u(R_{p_2})\, R_{p_2}\, (r_{p_2} + r_{p_4}) - u(R_{p_1})\, R_{p_1}\, (r_{p_1} + r_{p_3})] \\ &= \mathrm{p}_z \sin(\Delta\theta) \sin(\theta_{p_1} + \Delta\theta/2) \cos(\Delta\theta/2)\, \left[u(R_{p_2})\, R_{p_2}^2 - u(R_{p_1})\, R_{p_1}^2 \right]. \end{aligned}$$

Definition of the zonal mass in the r-z coordinate system gives

$$\tilde{m}_z = \rho_z V_z = \rho_z \left(R_{p_1}^2 \Delta R + R_{p_1} (\Delta R)^2 + \frac{(\Delta R)^3}{3} \right) \sin(\Delta\theta) \cos(\Delta\theta/2) \sin(\theta_{p_1} + \Delta\theta/2).$$

Comparing the last two formulas, we observe that three factors depending on θ_{p_1} and $\Delta\theta$ are canceled out giving the one-dimensional energy equations in absence of artificial viscous forces.

Symmetry analysis for viscous forces is more involved. We break the sum over points into two pieces. Using formulas (5.12) and the mirror symmetry of reference vectors $(\mathbf{F}_z^{ref})^{p_1}$ and $(\mathbf{F}_z^{ref})^{p_3}$ with respect to y-axis, we get the following references forces:

$$(\mathbf{f}_{ref}^{vis})_z^{p_1} = \begin{bmatrix} a \\ b \end{bmatrix}, \qquad (\mathbf{f}_{ref}^{vis})_z^{p_3} = \begin{bmatrix} -a \\ b \end{bmatrix},$$

where a and b are some numbers depending on R_{p_1} and $\Delta\theta$. Using formula (5.8), we get

$$\begin{aligned} \sum_{i=1,3} r_{p_i} (\mathbf{f}_{ref}^{vis})_z^{p_i} \cdot (\mathbf{u}^{ref})^{p_i} &= b\, u(R_{p_1})\, R_{p_1} (\sin\theta_{p_1} + \sin(\theta_{p_3})) \\ &= 2\, b\, u(R_{p_1})\, R_{p_1} \sin(\theta_{p_1} + \Delta\theta/2) \cos(\Delta\theta/2). \end{aligned}$$

A similar formula (with different b and R_{p_2} in place of R_{p_1}) is obtained for contribution from points p_2 and p_4. Comparing the result with formula for the zonal mass, we conclude that the factor depending on θ_{p_1} is canceled out giving a spherically symmetric method.

6 Approximation properties of $\mathcal{DIV}_\mu \mathcal{GRAD}$ operator

We consider three sequences of meshes shown in Fig.3. The first sequence (see Fig. 3a)) is obtained by applying the smooth mapping

$$\mathbf{x} := \mathbf{x} + 0.1 \sin(2\pi x) \sin(2\pi y)$$

to a square mesh. The second sequence (see Fig. 3b)) starts with a logically square 8×8 mesh and is built via its uniform refinement. The third sequence (see Fig. 3c)) consists of median meshes that are dual to Delaunay meshes build using points of meshes from the first sequence.

First, we analyze numerically approximation properties of discrete operator $\mathcal{DIV}_\mu \mathcal{GRAD}$ with $\mu = 1$. Let us consider a smooth velocity field $\mathbf{u}(x, y) = (\cos(\pi(x+y), \cos(\pi(x-y)))^T$ proposed in [21] and the corresponding discrete vector $\mathbf{U}$. The last three columns in Table 1 show a relative discrete L^2-norm of error between the discrete counterpart of $\tilde{\mathbf{f}}^{vis} = \mathrm{div}\,(\nabla\,\mathbf{u})$ and $\mathcal{DIV}\ \mathcal{GRAD}\,\mathbf{U}$. On smooth meshes (sequence number one), the convergence rate for this error approaches two. For piecewise smooth meshes (sequence number two), the convergence rate is one. For polygonal meshes, that were built using a smooth distribution of points, the convergence rate approaches 0.5.

In Fig. 4, we plot viscous forces at mesh points on different types of meshes. These meshes have about the same number of zones; however, the polygonal mesh has twice more points which results in a denser graphics.

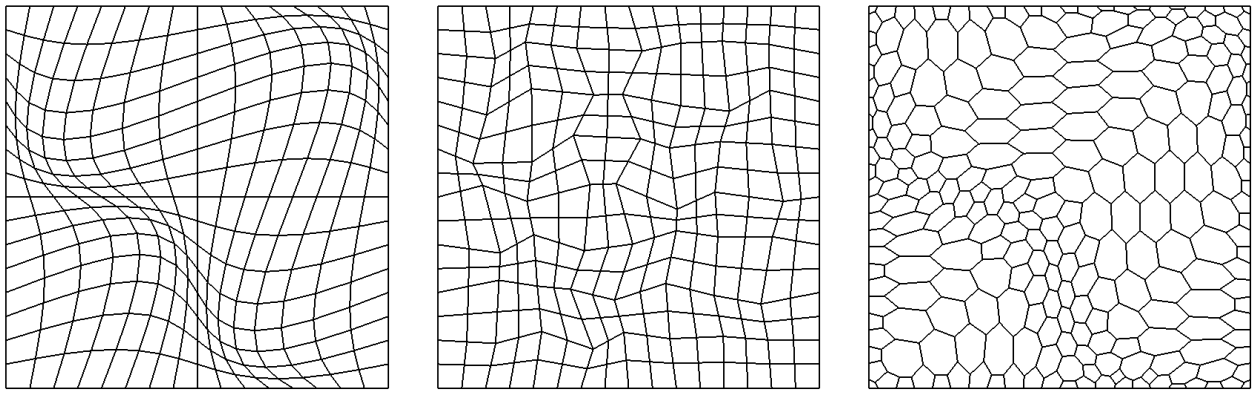

a) b) c)

Figure 3: Three representative meshes corresponding to the refinement level one.

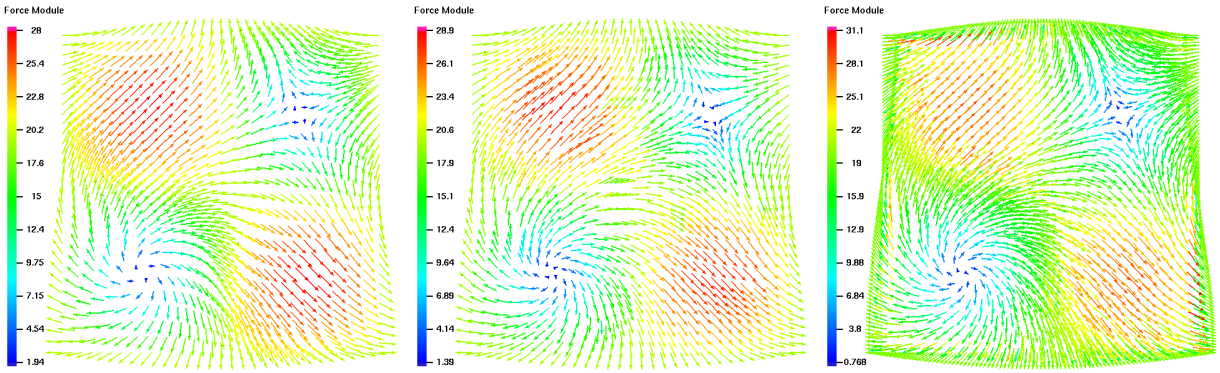

Figure 4: Form left to right: discrete viscous forces for $\mu = 1$ on smooth, random and polygonal meshes corresponding to the refinement level two.

Refinement level	Smooth	Random	Polygonal
0	8.12e-2	1.20e-1	1.48e-1
1	3.65e-2	7.86e-2	1.26e-1
2	1.16e-2	3.72e-2	9.61e-2
3	3.16e-3	1.65e-2	7.06e-2
4	8.15e-4	7.42e-3	5.03e-2
rate	1.68	1.03	0.39

Table 1: Relative L^2-norm of error between the discrete and analytic forces for $\mu = 1$.

Now we consider the same velocity field but a variable tensor μ:

$$\mu(x,y) = \mathcal{R}_{\pi/6} \begin{bmatrix} e^{-(x+y-1)^2/\nu_1} & 0 \\ 0 & e^{-(x-y)^2/\nu_2} \end{bmatrix} \mathcal{R}^T_{\pi/6}, \qquad \nu_1 = 1, \quad \nu_2 = 0.2.$$

The discrete viscous forces are shown in Fig. 5 for the meshes corresponding to the

refinement level two. The relative errors are collected in Table 2. We observe the same tendency in error reduction as for the case of constant μ.

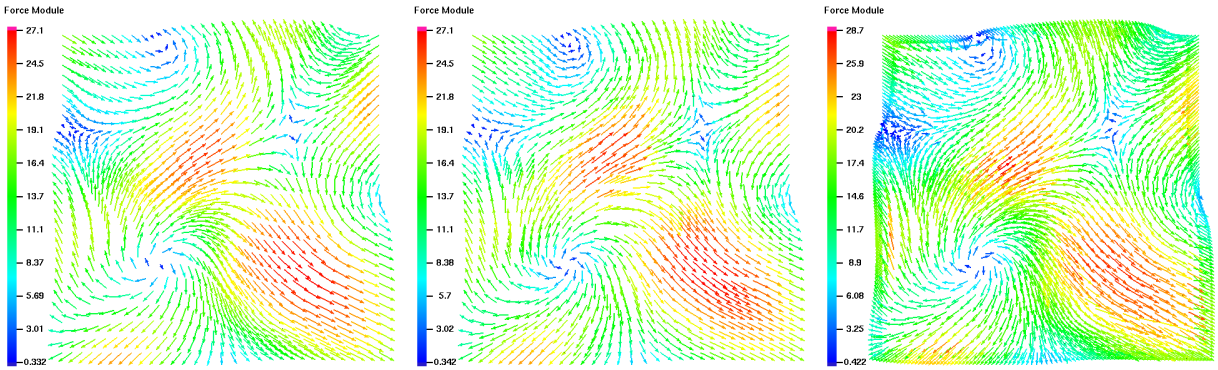

Figure 5: Form left to right: discrete viscous forces for variable μ on smooth, random and polygonal meshes corresponding to the refinement level two.

Refinement level	Smooth	Random	Polygonal
0	9.21e-2	1.39e-1	1.61e-1
1	3.78e-2	7.85e-2	1.32e-1
2	1.15e-2	3.58e-2	9.34e-2
3	3.08e-3	1.56e-2	6.62e-2
4	7.87e-4	6.89e-3	4.65e-2
rate	1.75	1.10	0.46

Table 2: Relative L^2-norm of error between the discrete and analytic forces for variable μ.

Let us note that for $\mu = 1$ and linear $\mathbf{u}$, the error is zero on an arbitrary mesh by construction. This is no longer true for a variable μ; thus, a non-zero numerical viscosity can be generated for a flow with uniform compression (linear $\mathbf{u}$). This problem is usually addressed by introducing an additional limiter as part of the coefficient μ_z, such that it reflects smoothness of the velocity field and vanishes for linear velocity field. Development of robust limiters for unstructured meshes is a challenging problem; therefore, no such limiters are used in our simulations. Instead, we try to control smoothness of the viscosity coefficient.

7 Numerical Hydro Experiments

The simulations we done using the code described in [7, 8, 9].

7.1 Computational meshes

Seven meshes are used in numerical experiments. All meshes are located in the first quadrant of the $\Re^2$ plane. At least two boundaries are attached to the coordinate axes. Symmetry boundary conditions are used on these boundaries.

PLU A uniform polar mesh with 50 zones radially and 30 zones angularly. The initial radius of the mesh is 1.

PLN A polar mesh with the same resolution as **PLU** but with non-uniform angular mesh steps. The steps between neighboring cells increase monotonically by 1%. The terminal zones in each polar layer have roughly 25% difference in the angular size.

SQR A square mesh with 50x50 zones. The initial domain is the unit square.

REC A rectangular mesh with 100x50 zones. The initial domain is the the unit square.

AMR A block structured mesh consisting of two uniform polar meshes with 25 zones radially both and 8 and 16 zones angularly, respectively. The initial radius of the first mesh is 0.5. The second mesh has initially the interior radius 0.5 and the exterior radius 1.

GEN A shape-regular polygonal mesh with 775 zones with 4 to 6 vertices. The initial radius of computational domain is 1. The initial mesh has shape-regular zones and roughly 30 zones in the radial direction.

SAL A logically rectangular mesh in domain $[0;\, 0.1] \times [0;\, 1]$ with 100 zones in the longest direction and 10 zones in the other direction. The coordinates of mesh points are the functions of they logical coordinates i, j:

$$x_{i,j} = (i-1)\Delta x + (11-j)\sin\Big(\frac{\pi(i-1)}{100}\Big)\Delta y, \qquad y_{i,j} = (j-1)\Delta y,$$

where $\Delta x = 1/100$ and $\Delta y = 0.1/10$.

The visualization was performed using the GMV package [1]. To plot isolines, GMV interpolates zonal unknowns to points which results in mild smoothing of data. In scattered plots, the zonal unknowns are assigned to zone centroids.

The developed tensor viscosity does not control hourglass distortion of zones. In some experiments, it is used in conjunction with the temporary triangular subzoning (TTS) method [6]. We found out that both methods may be required in experiments using all meshes except **PLU**. We tested three selections of the characteristic length summarized in Table 3 (see Section 3.4 for details). Better results were obtained using the choice shown in the table. Two Jacobi iterations are used to smooth variations of L_z^u only for the Noh problem on mesh **GEN** in the r-z coordinate system.

	PLU	**PLN**	**SQR**	**REC**	**AMR**	**GEN**	**SAL**
Noh	$\min(L_z^a, L_z^u)$	$\min(L_z^a, L_z^u)$	L_z^a	L_z^a	$\min(L_z^a, L_z^u)$	L_z^u	—
Sedov	L_z^u	L_z^u	L_z^a	L_z^a	L_z^u	L_z^u	—
Saltzman	—	—	—	—	—	—	L_z^a

Table 3: The characteristic length.

7.2 Noh implosion problem

In the Noh problem [25], an ideal gas with $\gamma = 5/3$, density $\rho = 1.0$, and pressure $p = 0$ is given an initial unit inwards radial velocity. A circular shock wave is generated at the origin and moves with constant speed 1/3. At time $t = 0.6$, the shock wave has radial coordinate 0.2. The density behind shock is 4^d, where $d = 2$ for the $x - y$ coordinate system and $d = 3$ in the $r - z$ coordinate system.

Figures 6–8 present results for the Noh problem with cylindrical symmetry. The CFL number is 0.2 in all experiments. The comparison is organized in pairs. First, two polar meshes are compared in Fig. 6. Part of mesh ahead of the shock has been removed for visualization clarity. The left panel verifies that the symmetry is preserved on the uniform mesh. The right panel shows that even small variation of mesh symmetry is sufficient to observe essential solution variation in the angular direction.

Second, two Cartesian meshes are compared in Fig. 7. The left panel illustrates preservation of mirror symmetry (with respect to line $x = y$). The right panel shows more accurate solution with smaller oscillations behind the shock due to better space resolution in the x-direction. Even small aspect ratio of zones in the **REC** mesh triggers development of hourglass modes. Therefore, the TTS method is used to damp these modes.

Finally, results for two advanced meshing strategies (**AMR** and **GEN**) are shown in Fig. 8. Lack of smoothness of density profiles is related to selection of the characteristic length L_z. For the **AMR** mesh, we observe shock cooling when it hits the interface between too meshes with sharp change in the size of neighboring zones. However, the solution is almost symmetric, density variation in the angular direction is in the fifth digit. For the **GEN** mesh, we observe cooling effect near boundaries $x = 0$ and $y = 0$ due to variation of the characteristic length. Note that a rigorous analysis of an optimal viscosity coefficient μ_z is beyond the scope of this article.

Figures 9–11 present results for the Noh problem with spherical symmetry. The CFL number is 0.2 in all experiments. We observe bigger relative error in density compared to the x-y coordinate system. However, the relative oscillations in scattered plots (symmetry violation) are only slightly worser, except for the simulation on the mesh **GEN**. We use two Jacoby iterations to smooth the characteristic length L_z^u and to reduce strong cooling effect around the z-axis. The polygonal mesh has roughly 40% lesser number of zones in the radial direction compared to the other meshes. Thus, all problems related to viscosity imperfections must be accentuated on this mesh.

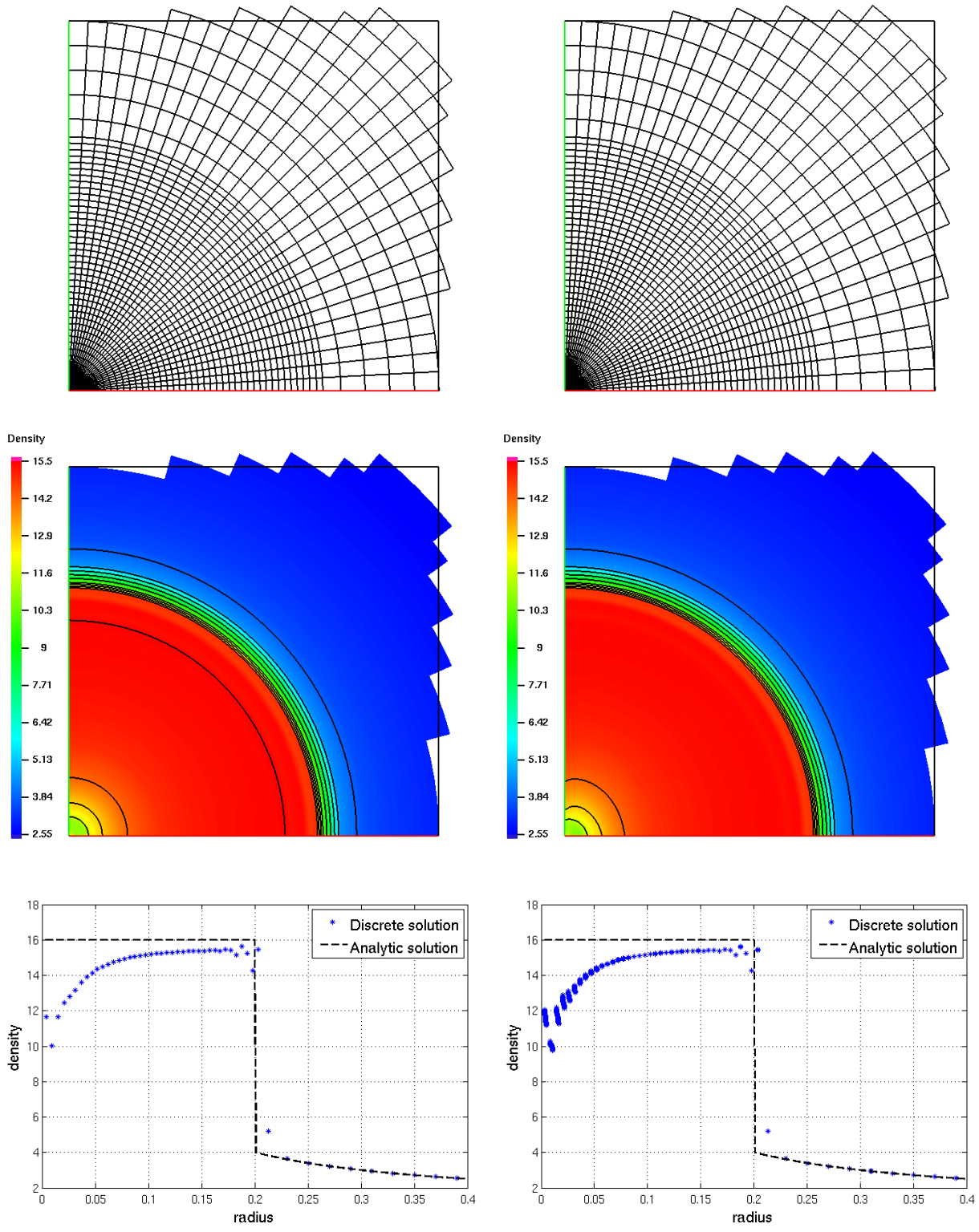

Figure 6: The Noh implosion problem in the x-y coordinate system on **PLU** (left panel) and **PLN** (right panel) meshes. Each panel shows the final mesh (top), density isolines (middle) and solution as the function of distance (bottom, stars). Part of mesh ahead of shock has been removed for visualization clarity. No TTS method is used.

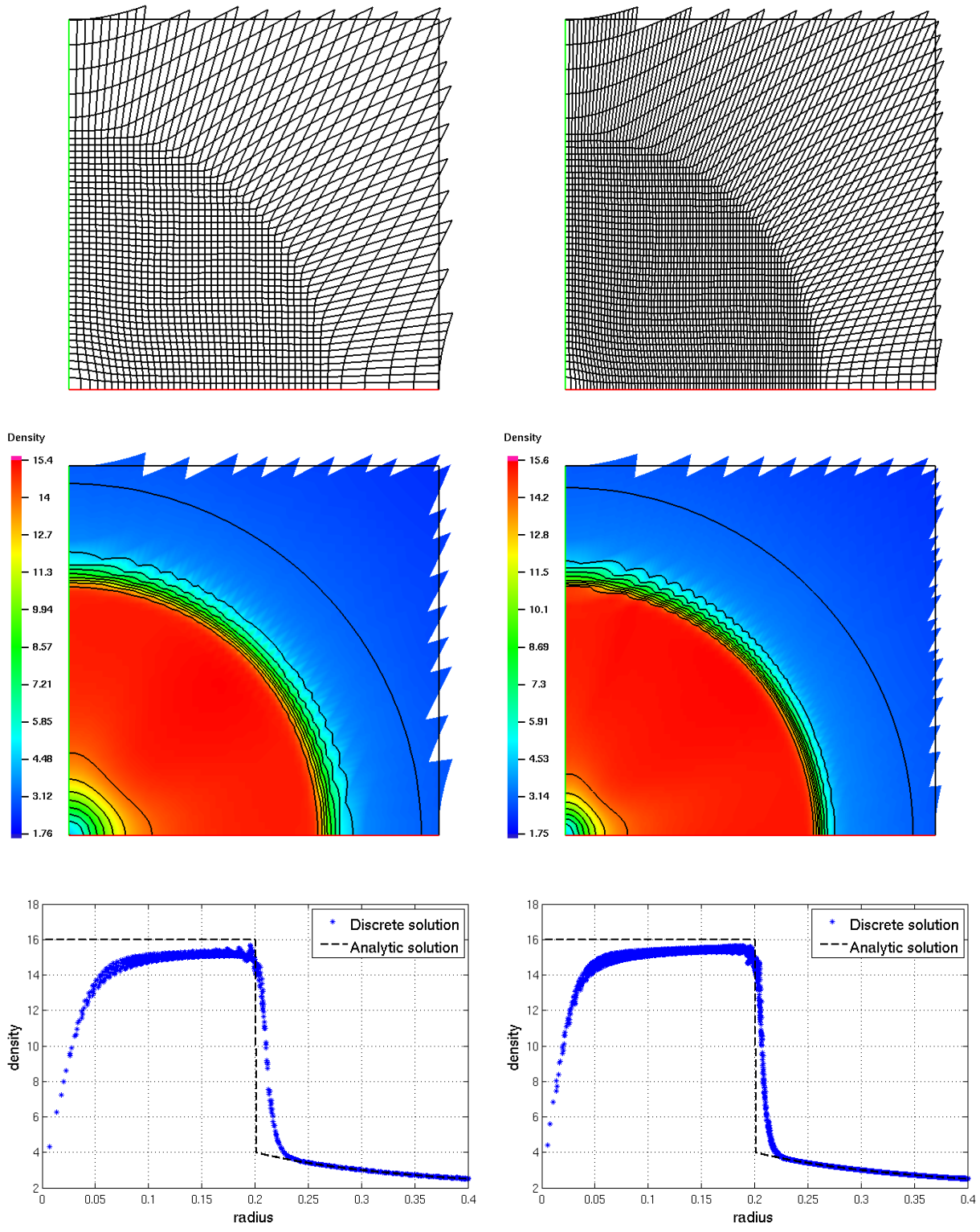

Figure 7: The Noh implosion problem in the x-y coordinate system on **SQR** (left panel) and **REC** (right panel) meshes. Each panel shows the final mesh (top), density isolines (middle) and solution as the function of distance (bottom, stars). Part of mesh ahead of shock has been removed for visualization clarity. The TTS method is used on **REC** mesh.

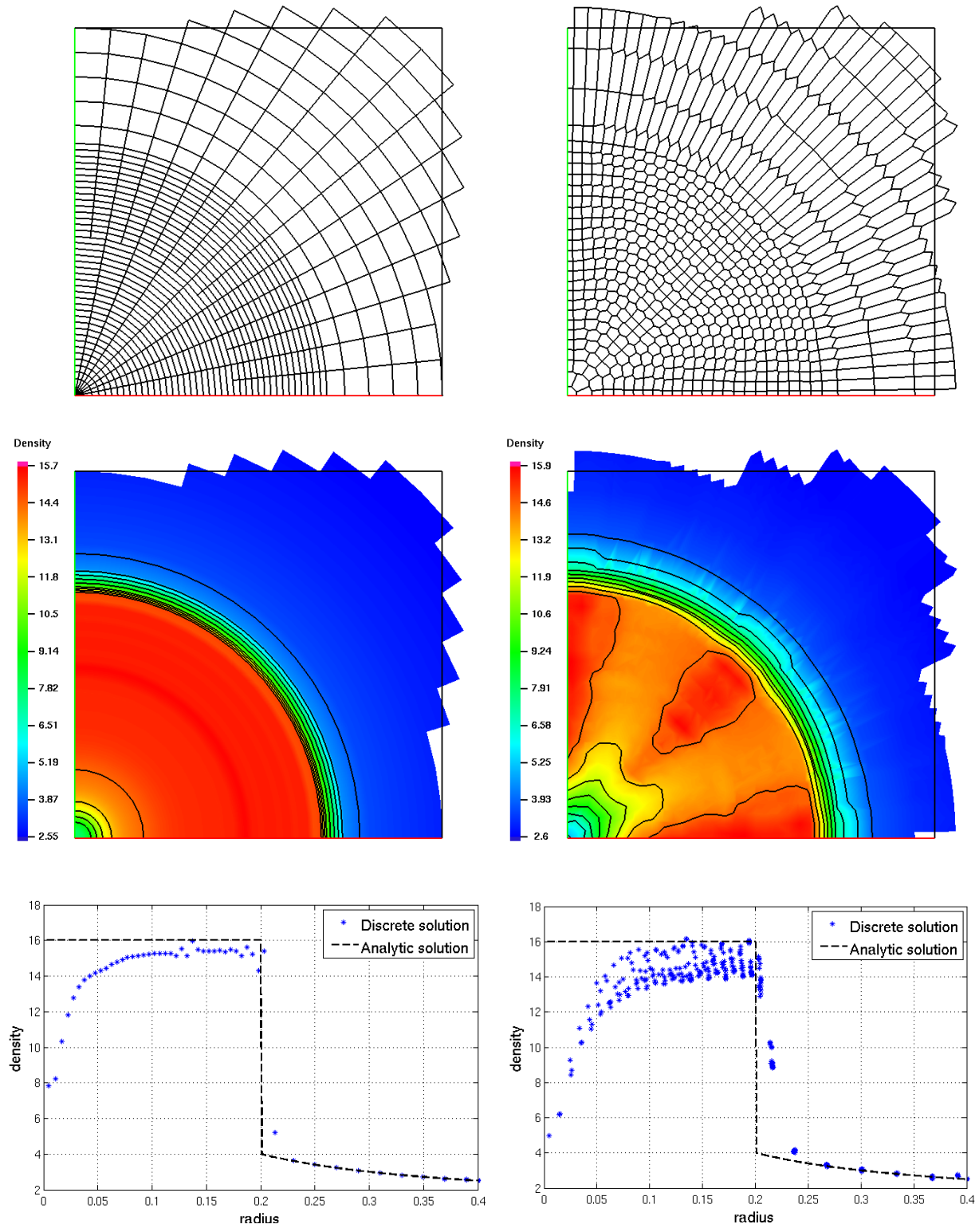

Figure 8: The Noh implosion problem in the x-y coordinate system on **AMR** (left panel) and **GEN** (right panel) meshes. Each panel shows the final mesh (top), density isolines (middle) and solution as the function of distance (bottom, stars). Part of mesh ahead of shock has been removed for visualization clarity. The TTS method is used on both meshes.

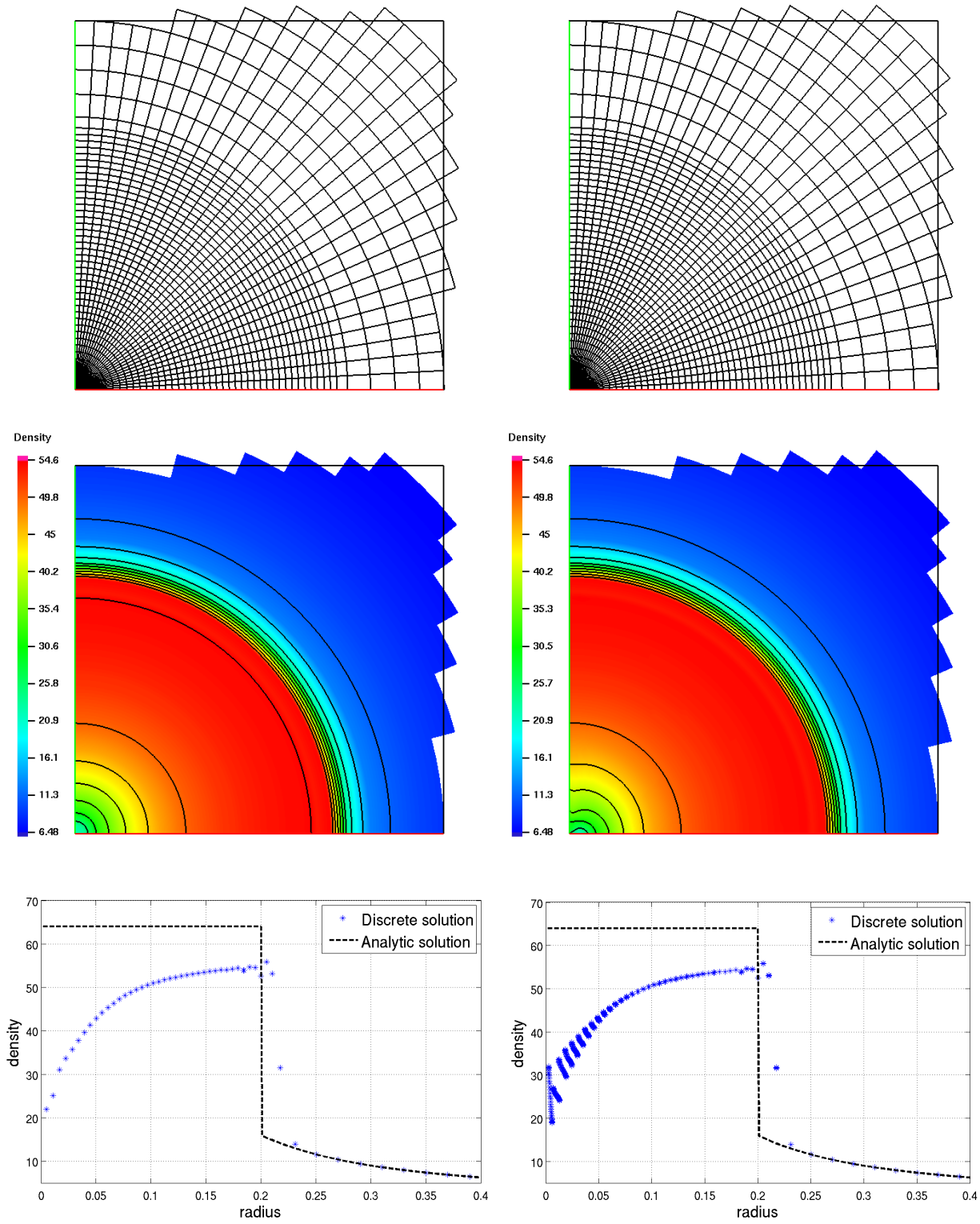

Figure 9: The Noh implosion problem in the r-z coordinate system on **PLU** (left panel) and **PLN** (right panel) meshes. Each panel shows the final mesh (top), density isolines (middle) and solution as the function of distance (bottom, stars). Part of mesh ahead of shock has been removed for visualization clarity. The TTS method is used on **PLN** mesh.

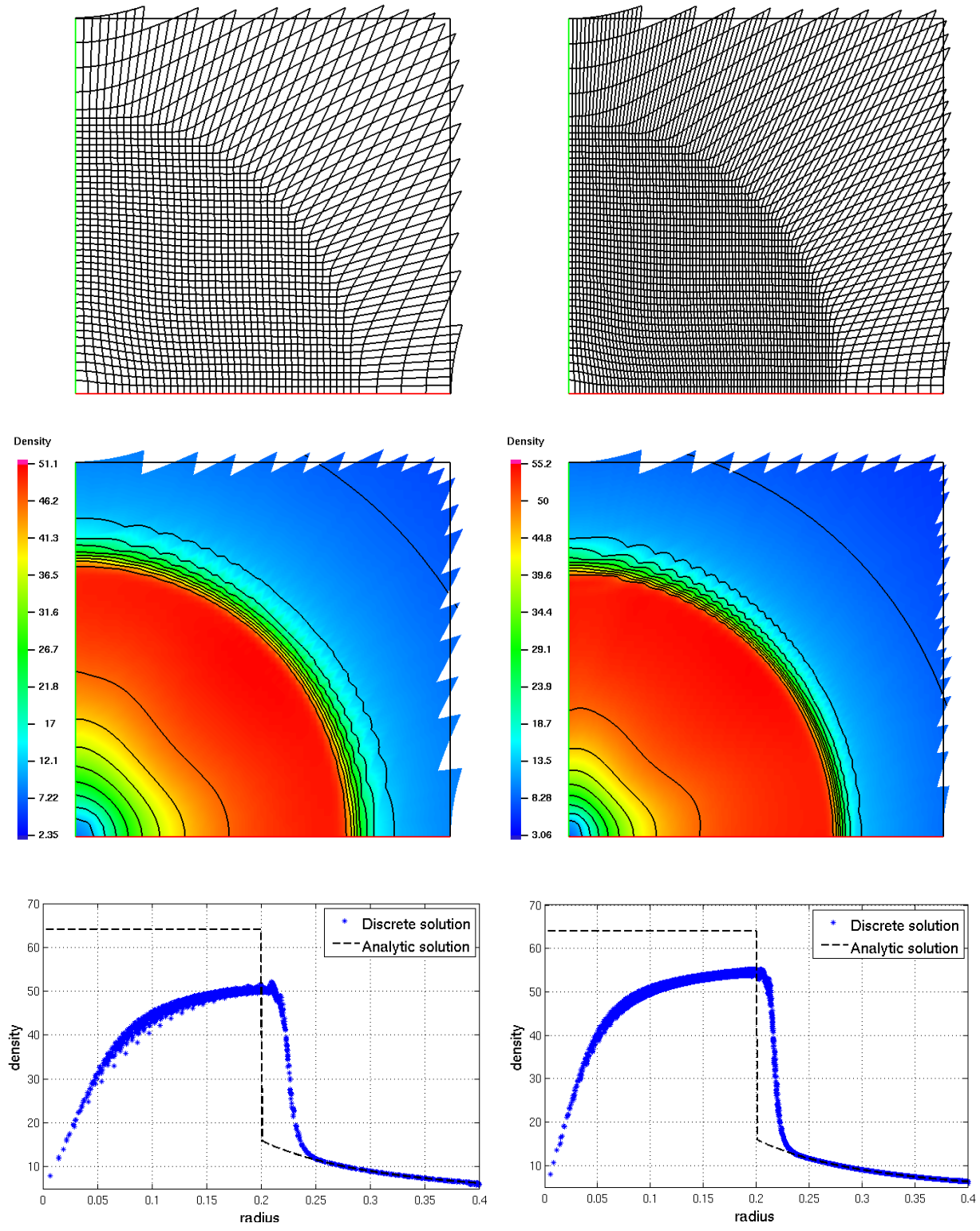

Figure 10: The Noh implosion problem in the r-z coordinate system on **SQR** (left panel) and **REC** (right panel) meshes. Each panel shows the final mesh (top), density isolines (middle) and solution as the function of distance (bottom, stars). Part of mesh ahead of shock has been removed for visualization clarity. The TTS method is used on the **REC** mesh.

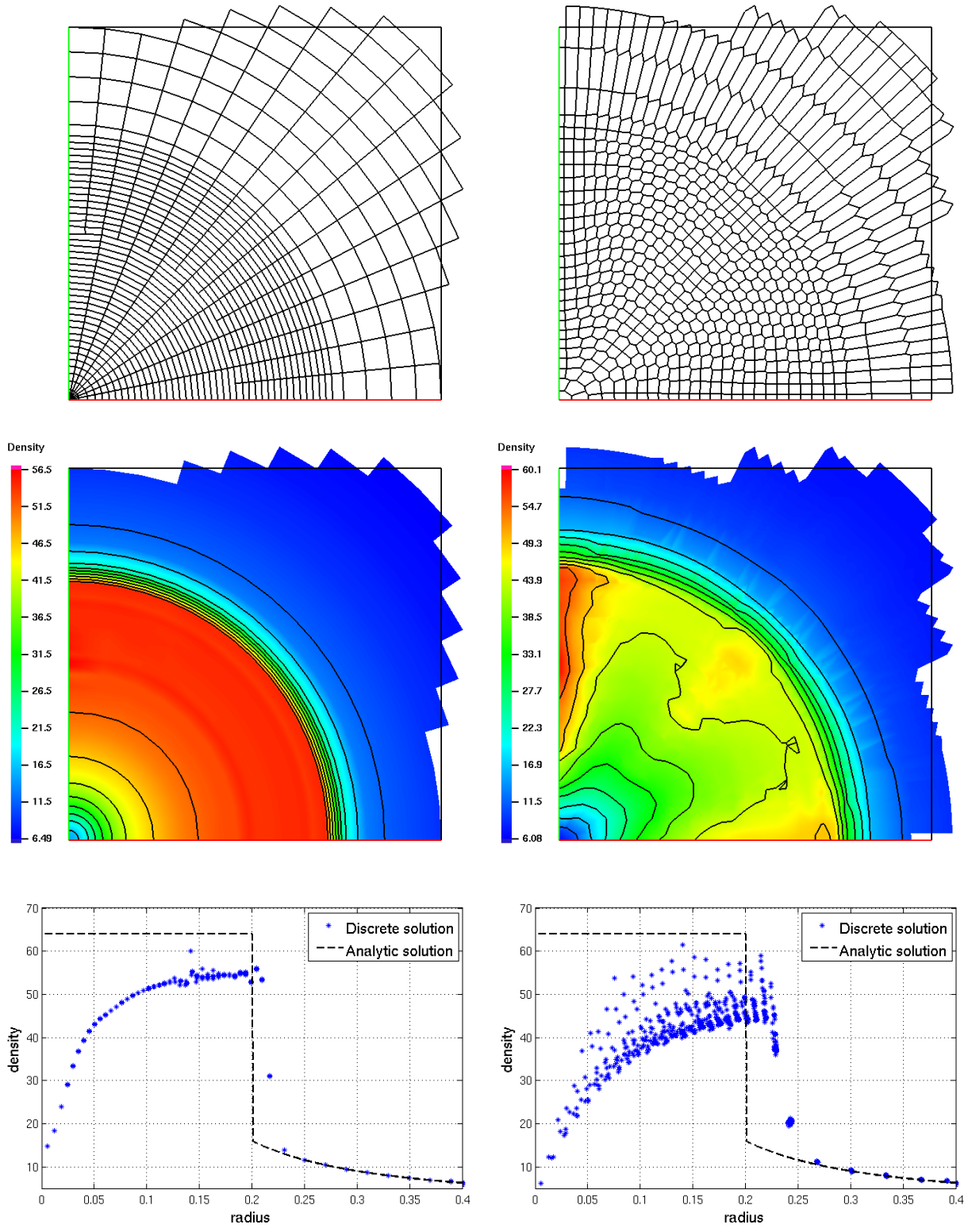

Figure 11: The Noh implosion problem in the r-z coordinate system on **AMR** (left panel) and **GEN** (right panel) meshes. Each panel shows the final mesh (top), density isolines (middle) and solution as the function of distance (bottom, stars). Part of mesh ahead of shock has been removed for visualization clarity. The TTS method is used in both experiments.

7.3 Sedov blast wave problem

The Sedov explosion problem [20, 27, 28] generates a strong diverging shock wave. The initial density of the gas with $\gamma = 1.4$ is one and the initial velocity is zero. At $t = 0$, the total energy E_0 is all internal and concentrated at the origin. The analytical solution gives the expanding shock of radius r_d with a peak density of 6,

$$r_d = \left(E_0/(\alpha_d\,\rho_0)\right)^{1/(2+d)}\, t^{2/(2+d)},$$

where d is the geometry parameter, $d = 2, 3$, $\alpha_2 = 0.983909$ and $\alpha_3 = 0.850937$. The total energy E_0 is defined such that $r_d = 0.9$ at time $t = 1$. In numerical experiments, a few zones near the origin are given the constant specific internal energy. We use only one zone for meshes **SQR** and **GEN**. We use two zones for mesh **REC** that form the square region near the origin.

Figures 12–14 present results for the Sedov problem with cylindrical symmetry. The CFL number is 0.2 in all experiments. The comparison is organized in pairs. First, two polar meshes are compared in Fig. 12. The left panel verifies that the symmetry is preserved on the uniform mesh. The right panel shows that with help of the TTS method, we get moderate mesh distortion from the radial structure. Without that method, the hourglass distortion is developed behind the shock and results in mesh tangling around $t = 0.7$.

Second, two Cartesian meshes are compared in Fig. 13. The left panel illustrates preservation of mirror symmetry with respect to line $x = y$. The right panel shows more accurate solution due to better space resolution in the x-direction.

Finally, results for two advanced meshing strategies are shown in Fig. 14. Minor variations of density profiles (compare with the Noh problem) are observed in the region of **AMR** mesh where the angular resolution is doubled. The polygonal mesh has the smallest number of zones and still gives accurate solution.

Figures 15–17 present results for the Sedov problem with spherical symmetry. The CFL number is 0.2 in all experiments. On average, the results are only slightly worser than that in the x-y coordinate system.

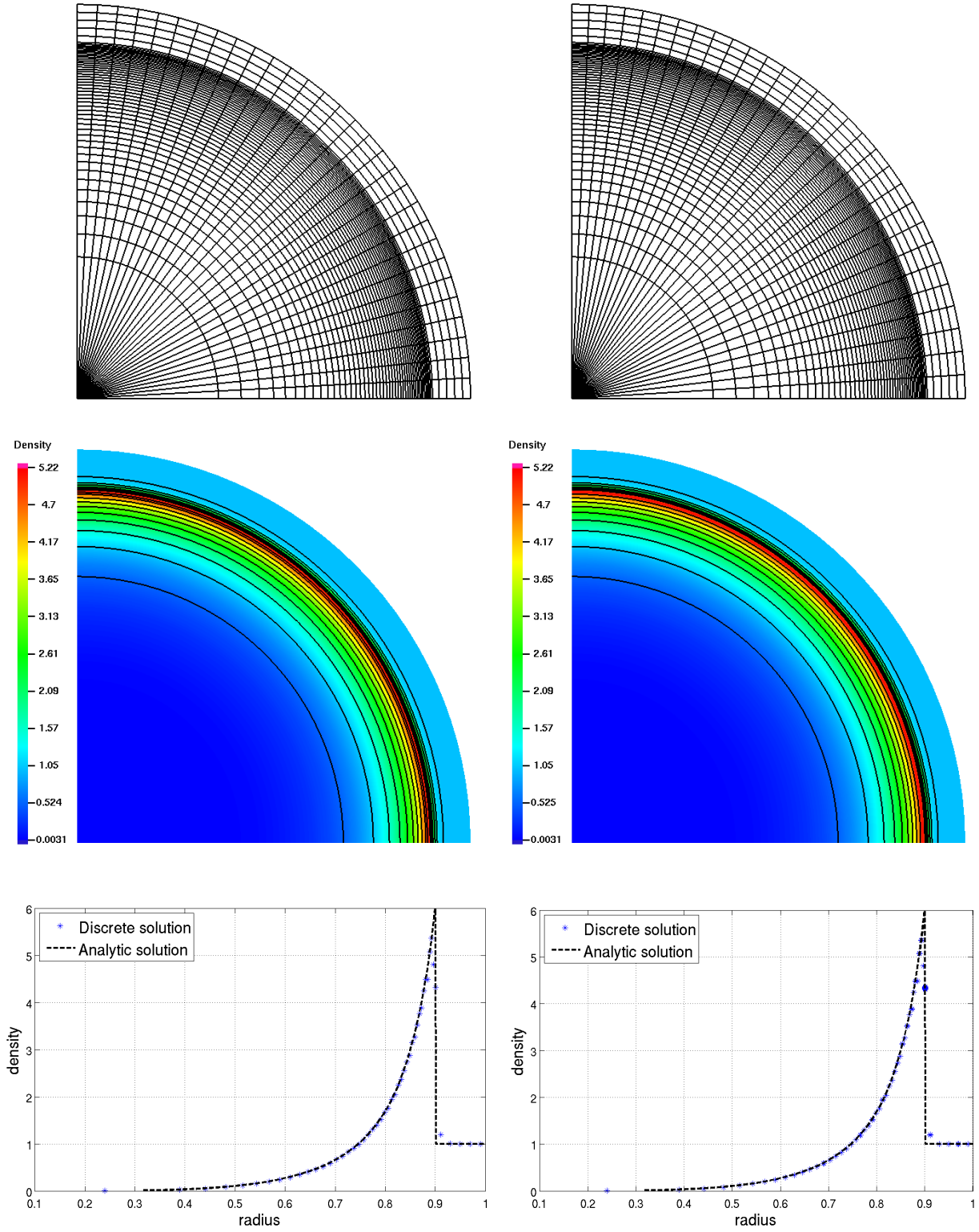

Figure 12: The Sedov explosion problem in the x-y coordinate system on **PLU** (left panel) and **PLN** (right panel) meshes. Each panel shows the final mesh (top), density isolines (middle) and solution as the function of distance (bottom, stars). The TTS method is used on mesh **PLN**.

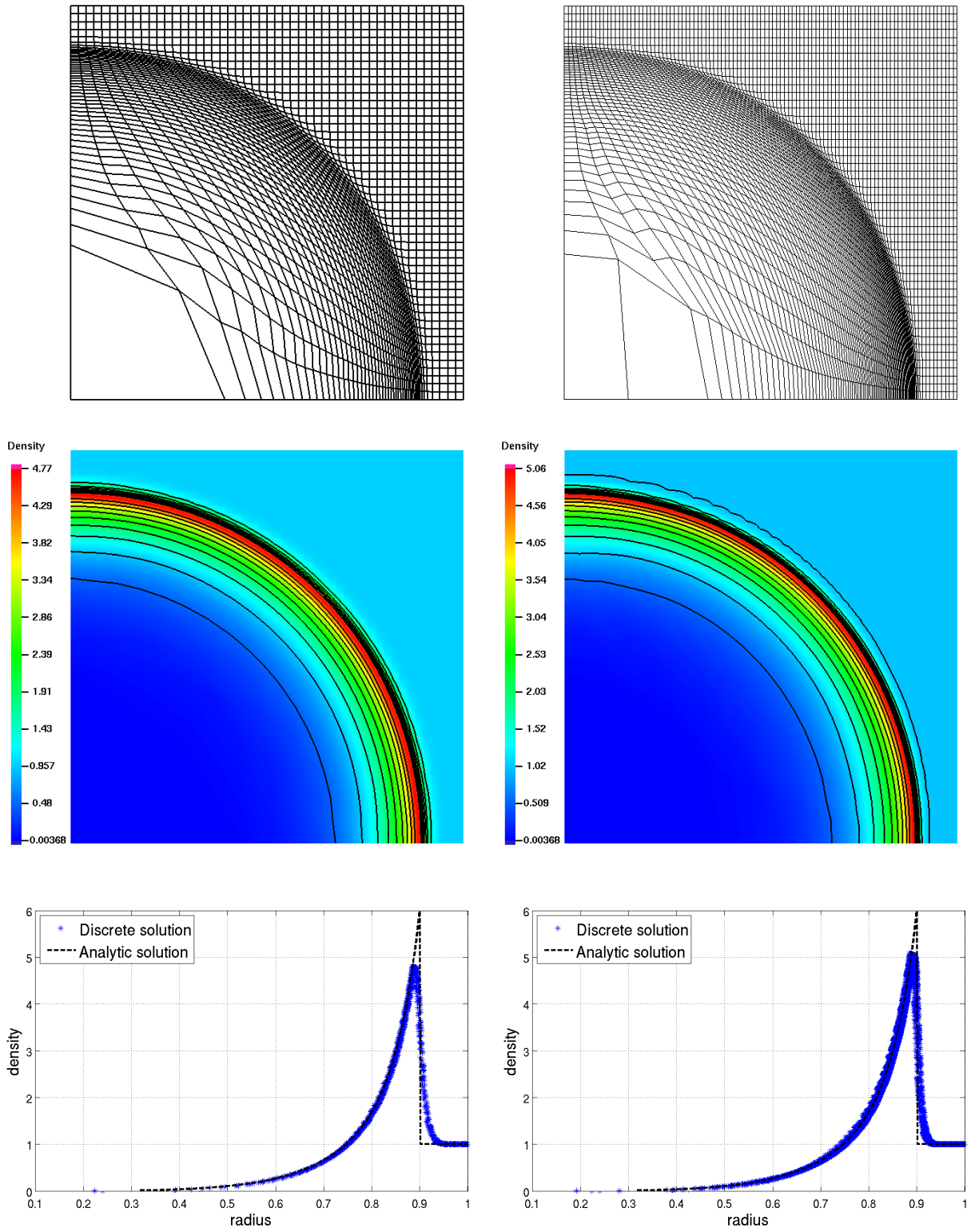

Figure 13: The Sedov explosion problem in the x-y coordinate system on **SQR** (left panel) and **REC** (right panel) meshes. Each panel shows the final mesh (top), density isolines (middle) and solution as the function of distance (bottom, stars). The TTS method is used in both simulations.

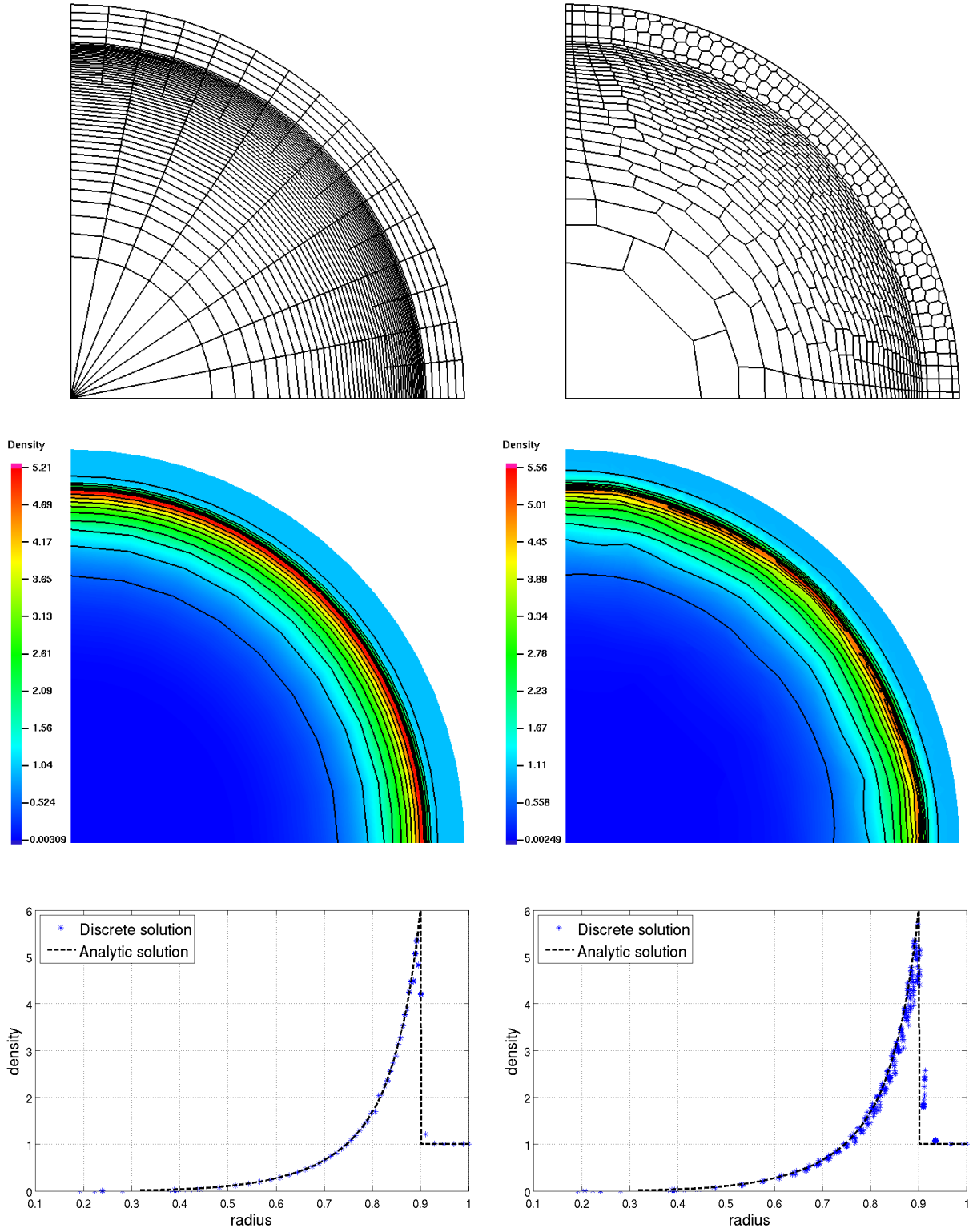

Figure 14: The Sedov explosion problem in the x-y coordinate system on **AMR** (left panel) and **GEN** (right panel) meshes. Each panel shows the final mesh (top), density isolines (middle) and solution as the function of distance (bottom, stars). The TTS method is used on mesh **GEN**.

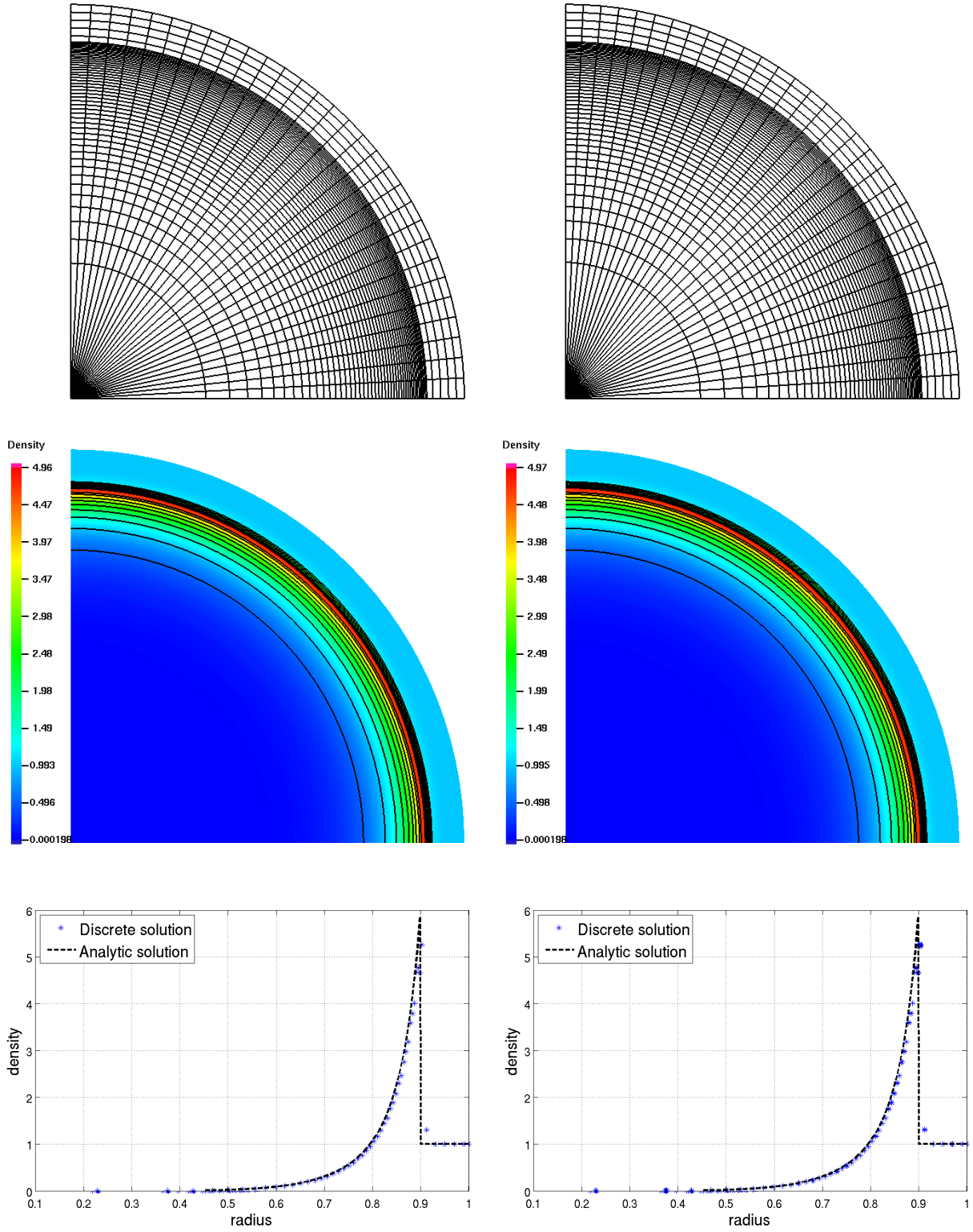

Figure 15: The Sedov explosion problem in the r-z coordinate system on **PLU** (left panel) and **PLN** (right panel) meshes. Each panel shows the final mesh (top), density isolines (middle) and solution as the function of distance (bottom, stars). The TTS method is used on mesh **PLN**.

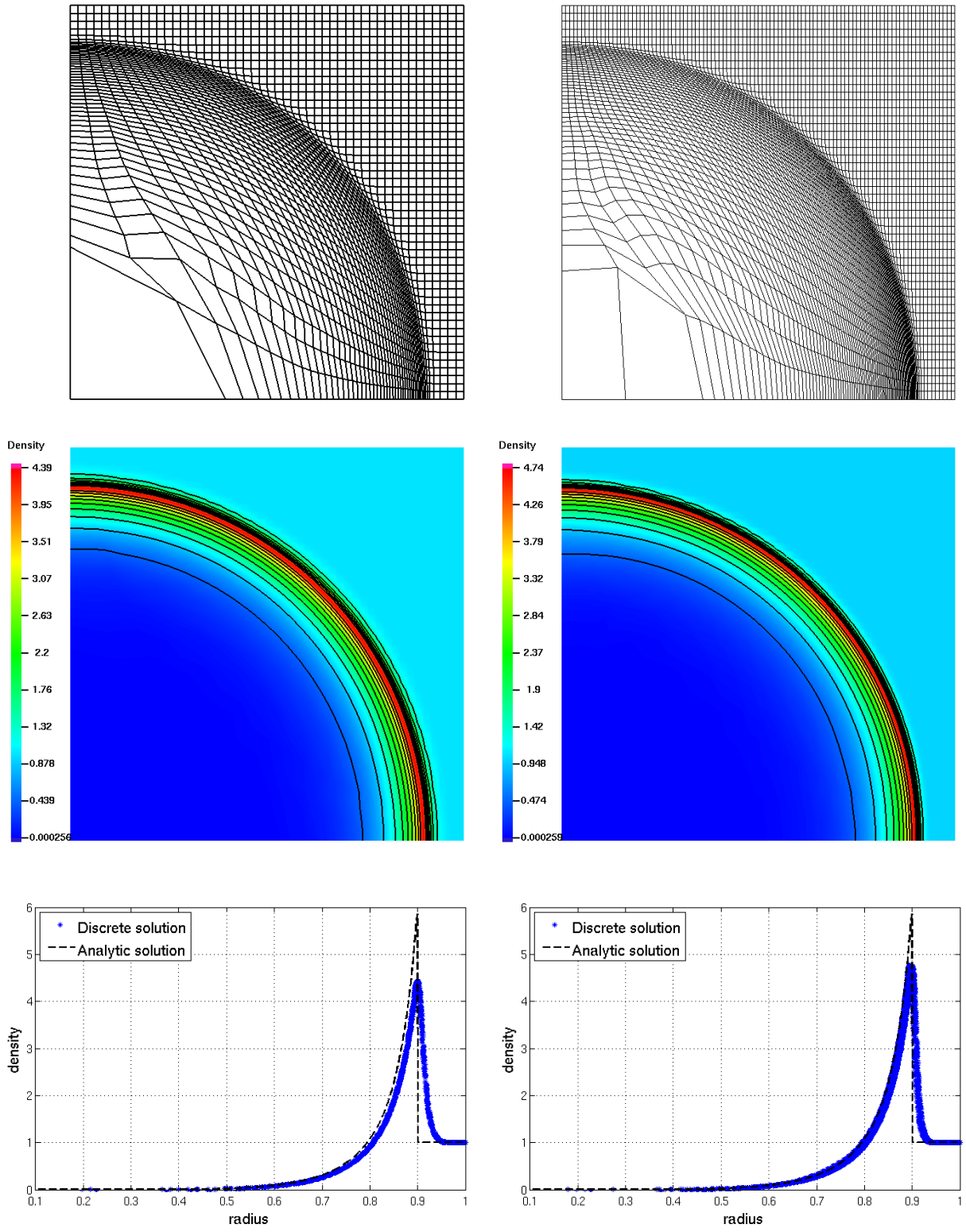

Figure 16: The Sedov explosion problem in the r-z coordinate system on **SQR** (left panel) and **REC**(right panel) meshes. Each panel shows the final mesh (top), density isolines (middle) and solution as the function of distance (bottom, stars). The TTS method is used in both simulations.

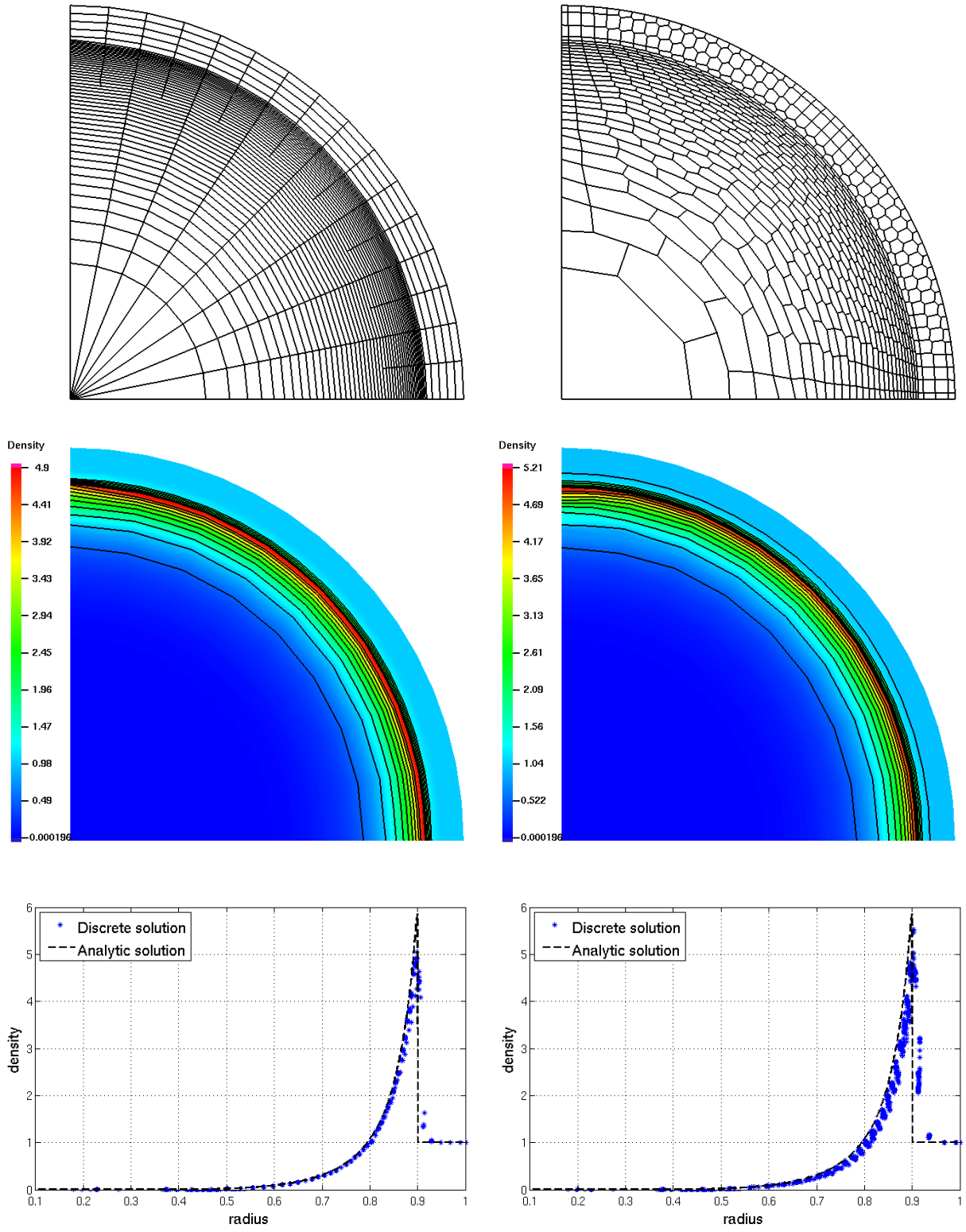

Figure 17: The Sedov explosion problem in the r-z coordinate system on **AMR** (left panel) and i**GEN** (right panel) meshes. Each panel shows the final mesh (top), density isolines (middle) and solution as the function of distance (bottom, stars). The TTS method is used in both simulations.

7.4 Saltzman piston problem

In the Saltzman problem, a one-dimensional shock wave propagates through a two-dimensional mesh [26, 14]. This tests the ability of the method to model shock waves that are oblique to the mesh. As artificial viscosity is dominant in the shock wave propagation, the Saltzman piston problem is often used for testing new viscosity methods.

A box is initially filled with the cold ideal gas ($\gamma = 5/3$) at density 1. A piston moves into the box with a constant speed 1.0 and generates a shock wave that reflects from the opposite fixed end of the box at time $t = 0.8$ and hits the piston at time $t = 0.9$. The simulation time is 0.925 when the shock reflected from the piston has not yet reached the fixed end. The final density behind the shock is 20 and the density ahead of the shock is 10 in both coordinate systems.

Figure 18 compares results of simulations in the x-y and r-z coordinate systems. We observe more accurate results in the r-z coordinate system. The final mesh lines are more straight in this experiment. A common wall heating effect is observed on the top wall of the box where the symmetry boundary condition is applied.

8 Conclusion

We constructed a new mimetic tensor artificial viscosity on general polygonal meshes. The tensor viscosity is designed as discretization of the differential operator $\mathrm{div}\,(\mu\nabla\mathbf{u})$, where μ is the full fourth-order tensor coefficient. We described how the new artificial viscosity can be incorporated into the staggered discretization of Lagrangian hydrodynamics in both the Cartesian and axisymmetric geometries. We proved that the new tensor viscosity preserves symmetry on special meshes. We demonstrated performance of the new viscosity on a set of test problems.

In future papers, we are planning to construct a tensor coefficient μ, which will reflect direction of the flow and develop limiters which will identify adiabatic compression and turn viscosity off for such flows.

Extension of the method to three dimensions will be described in a separate paper.

Acknowledgments

This work was carried out under the auspices of the National Nuclear Security Administration of the U.S. Department of Energy at Los Alamos National Laboratory under Contract No. DE-AC52-06NA25396. We authors acknowledge support of the DOE Office of Science Advanced Scientific Computing Research (ASCR) Program in Applied Mathematics Research and the Advanced Simulation & Computing (ASC) Program.

Authors thank B. Wendroff, R. Rieben and T.Kolev for fruitful discussions. Authors thank D. Burton, M. Bement and M. Kenamond for help with the FLAG code.

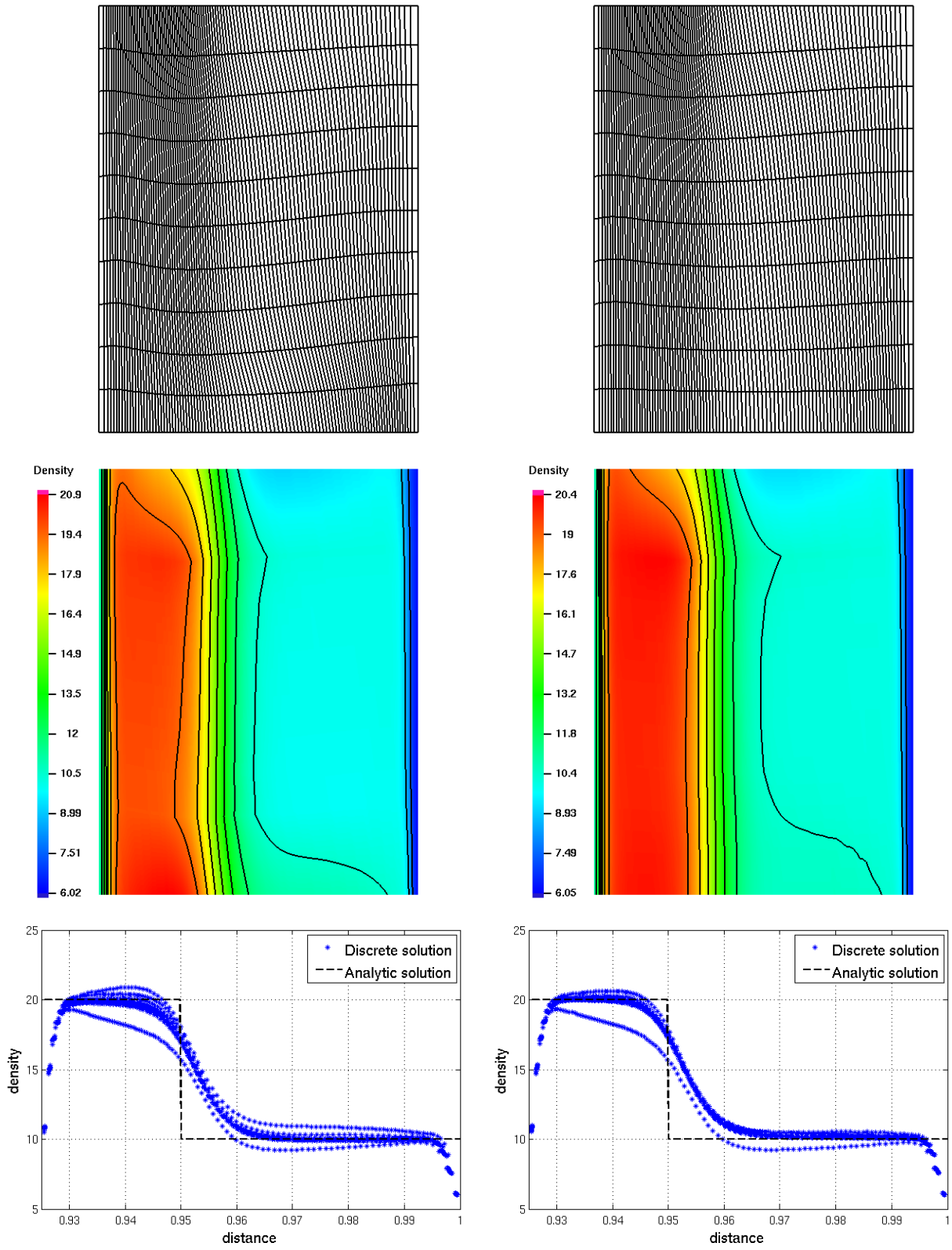

Figure 18: The Saltzman piston problem in the x-y (left panel) and r-z (right panel) coordinate systems on the mesh **SAL**. The z-axis is horizontal. Each panel shows the final mesh (top), density isolines (middle) and solution as the function of distance (bottom, stars). The TTS method is used in both experiments.

References

[1] General Mesh Viewer, version 4.5. Technical Report LA-UR-95-2986, Los Alamos National Laboratory, 1995.

[2] A. Barlow, D. Burton, M. Shashkov, and B. Wendroff. Compatible, energy and symmetry preserving 2d lagrangian hydrodynamics in rz - cylindrical coordinates. Technical Report LA-UR-09-05814, Los Alamos National Laboratory, 2009. see also: Proceedings of Conference on NUMERICAL METHODS for MULTI-MATERIAL FLUIDS and STRUCTURES, Pavia, Italy, September 21-29, 2009, `http://www.eucentre.it/multimat09/index.php`.

[3] F. Brezzi, A. Buffa, and K. Lipnikov. Mimetic finite differences for elliptic problems. *M2AN Math. Model. Numer. Anal.*, 43:277–295, 2009.

[4] F. Brezzi, K. Lipnikov, M. Shashkov, and V. Simoncini. A new discretization methodology for diffusion problems on generalized polyhedral meshes. *Comput. Methods Appl. Mech. Engrg.*, 196:3682–3692, 2007.

[5] F. Brezzi, K. Lipnikov, and V. Simoncini. A family of mimetic finite difference methods on polygonal and polyhedral meshes. *Math. Models Methods Appl. Sci.*, 15(10):1533–1551, 2005.

[6] P. Browne and K. Wallick. The reduction of mesh tangling in two-dimensional Lagrangian hydrodynamics codes by the use of viscosity, artificial viscosity, and TTS (temporary triangular subzoning for long, thin zones). Technical Report LA-470-MS, Los Alamos National Laboratory, 1971.

[7] D. Burton. Multidimensional discretization of conservation laws for unstructured grids. In *Second International Workshop on Analytical Methods and Process Optimization in Fluid and Gas Mechanics (SAMGOP), Arzamas-16, Russia (1994)*, 1994. Also Report UCRL-JC-118306, Lawrence Livermore National Laboratory.

[8] D. E. Burton. Exact conservation of energy and momentum in staggered-grid hydrodynamics with arbitrary connectivity. In *Advances in the Free Lagrange Method*. Springer-Verlag, New-York, 1990.

[9] D. E. Burton. Consistent finite-volume discretization of hydrodynamics conservation laws for unstructured grids. Technical report, Report UCRL-JC-118788, Lawrence Livermore National Laboratory, 1994.

[10] J. Campbell, J. M. Hyman, and M. Shashkov. Mimetic finite difference operators for second-order tensors on unstructured grids. *Computers & Mathematics with Applications*, 44:157–173, 2000.

[11] J. Campbell and M. Shashkov. A tensor artificial viscosity using a mimetic finite difference algorithm. *J. Comput. Phys.*, 172:739–765, 2001.

[12] E. Caramana, M. Shashkov, and P. Whalen. Formulation of artificial viscosity for multi-dimensional shock wave calculations. *J. Comput. Phys.*, 144:70–97, 1998.

[13] E. J. Caramana, D. E. Burton, M. J. Shashkov, and P. P. Whalen. The construction of compatible hydrodynamics algorithms utilizing conservation of total energy. *J. Comput. Phys.*, 146:227262, 1998.

[14] J. Dukowicz and B. Meltz. Vorticity errors in multidimensional lagrangian codes. *J. Comput. Phys.*, 99:115–134, 1992.

[15] V. Gyrya and K. Lipnikov. High-order mimetic finite difference method for diffusion problems on polygonal meshes. *J. Comput. Phys.*, 227:8841–8854, 2008.

[16] J. Hyman and M. Shashkov. Mimetic discretizations for Maxwell's equations and the equations of magnetic diffusion. *Progress in Electromagnetic Research*, 32:89–121, 2001.

[17] J. Hyman, M. Shashkov, and S. Steinberg. The numerical solution of diffusion problems in strongly heterogeneous non-isotropic materials. *J. Comput. Phys.*, 132:130–148, 1997.

[18] J. M. Hyman and M. Shashkov. Adjoint operators for the natural discretizations of the divergence, gradient and curl on logically rectangular grids. *Applied Numerical Mathematics*, 25:413–442, 1997.

[19] J. M. Hyman and M. Shashkov. Natural discretizations for the divergence, gradient, and curl on logically rectangular grids. *International Journal of Computers & Mathematics with Applications*, 33:81–104, 1997.

[20] J. R. Kamm. Evoluation of the Sedov-von Neumann-Taylor blast wave solution. Technical report, Report RLA-UR-00-6055, Los Alamos National Laboratory, 2000.

[21] T. Kolev and R. Rieben. A tensor artificial viscosity using a finite element approach. *J. Comput. Phys.*, 228(22):8336–8366, 2009.

[22] K. Lipnikov, J. Morel, and M. Shashkov. Mimetic finite difference methods for diffusion equations on non-orthogonal non-conformal meshes. *J. Comput. Phys.*, 199, 2004.

[23] L. Margolin, M. Shashkov, and P. Smolarkiewicz. A discrete operator calculus for finite difference approximations. *Comput. Methods Appl. Mech. Engrg.*, 187:365–383, 2000.

[24] J. Morel, R. Roberts, and M. Shashkov. A local support-operators diffusion discretization scheme for quadrilateral $r - z$ meshes. *J. Comput. Phys.*, 144:17–51, 1998.

[25] W. Noh. Errors for calculations of strong shocks using an artificial viscosity and an artificial heat flux. *J. Comput. Phys.*, 72:78–120, 1987.

[26] J. Saltzman and P. Colella. Second order corner coupled upwind transport methods for Lagrangian hydrodynamics. Technical report, LA-UR-85-678, Los Alamos National Laboratory, 1985.

[27] L. Sedov. *Similarity and Dimensional methods in mechanics.* Academic Press, New York, 1959.

[28] A. Shestakov. Time-dependent simulations of point explosion with heat conduction. *Physics of Fluids*, 11:1091–1095, 1999.

[29] Z. Warsi. *Fluid Dymanics. Theoretical and Computational Approaches.* CRC Press, Boca Raton, 1993.

[30] M. Wilkins. Use of artificial viscosity in multidimensional shock wave problems. *J. Comput. Phys.*, 36:281–303, 1980.